High Resolution 3D Winds Derived from a Modified WISSDOM Synthesis Scheme using Multiple Doppler Lidars and Observations

Chia-Lun Tsai[1], Kwonil Kim[1], Yu-Chieng Liou[2], and GyuWon Lee*[1]

[1]Department of Astronomy and Atmospheric Sciences, Center for Atmospheric REmote sensing (CARE), Kyungpook National University, Daegu, South Korea

[2]Department of Atmospheric Sciences, National Central University, Jhongli, Taiwan

* Corresponding author: Prof. GyuWon Lee, E-mail: gyuwon@knu.ac.kr

Abstract

A̶ The WISSDOM (Wind Synthesis System using Doppler Measurements) synthesis scheme was developed to derive high-resolution 3-dimensional (3D) winds under clear-air conditions. From this variational-based scheme, detailed wind information was obtained from scanning Doppler lidars, automatic weather stations (AWS), sounding observations, and local reanalysis datasets (LDAPS, Local Data Assimilation and Prediction System), which were utilized as constraints to minimize the cost function. The objective of this study is to evaluate the performance and accuracy of derived 3D winds from this modified scheme. A strong wind event was selected to demonstrate its performance over complex terrain in Pyeongchang, South Korea. The size of the test domain is 12×12 km^2 extended up to 3 km height mean sea level (MSL) with remarkably high horizontal and vertical resolution of 50 m. The derived winds reveal that reasonable patterns were explored from a control run, as they have high similarity with the sounding observations. The results of intercomparisons show that the correlation coefficients between derived horizontal winds and sounding observations are 0.97 and 0.87 for u- and v-component winds, respectively, and the averaged bias (root mean square deviation, RMSD) of horizontal winds is between −0.78 and 0.09 (1.77 and 1.65) m s^{-1}. The correlation coefficients between WISSDOM-derived winds and lidar QVP (quasi-vertical profile) are 0.84 and 0.35 for u- and v-component winds, respectively, and the averaged bias (RMSD) of horizontal winds is between 2.83 and 2.26 (3.69 and 2.92) m s^{-1}. The statistical errors also reveal a satisfying performance of the retrieved 3D winds; the median values of wind directions are −5~5 (0~2.5) degrees, the wind speed is approximately −1~3 m s^{-1} (−1~0.5 m s^{-1}) and the vertical velocity is −0.2~0.6 m s^{-1} compared with the lidar QVP (sounding observations). A series of sensitivity tests with different weighting coefficients, radius of influence (RI) in interpolation and various combination of different datasets were also performed. The results indicate that the present setting of the control run is the optimal reference to WISSDOM synthesis in this event and will help verify the impacts against various scenarios and observational references in this area.

1. Introduction

In the past few decades, many practical methods have been developed to derive wind information by using meteorological radar data (Mohr and Miller, 1983, Lee et al., 1994, Liou and Chang, 2009, Bell et al. 2012). The derived winds substantially revealed reasonable patterns compared with conventional observations (such as surface stations, soundings, wind profiles, etc.) and models (Liou et al., 2014, North et al., 2017, Chen, 2019, Oue et al., 2019). Most comprehensive applications of the derived winds were adopted to document kinematic and precipitation structures associated with various weather systems or phenomena at different scales from thousands [cold fronts and low-pressure systems (LPS)] over, hundreds (tropical cyclones and typhoons) to, and a couple of kilometers [convective lines and tropical cyclone rainbands (it naturally depends on the length and width of the rainbands)] , such as cold fronts, typhoons, tropical cyclone rainbands, convective lines, and nonprecipitation low-pressure systems (LPS) (Yu and Bond, 2002, Yu and Jou, 2005, Yu and Tsai, 2013, Yu and Tsai, 2017, Tsai et al. 2018, Yu et al., 2020, Cha and Bell, 2021, Tsai et al., 2022). In addition, the accuracy of 3D winds could be improved when increasing the numbers of Doppler radar because relatively fewer assumptions and more information can be included (Yu and Tsai 2010, Liou and Chang, 2009). Therefore, the retrieved schemes within multiple Doppler radars are a more popular way to obtain high-quality 3D winds and have been extensively applied to meteorological analyses.

The technique of velocity track display (VTD, Lee et al., 1994) and ground-based velocity track display (GBVTD, Lee et al., 1999) can derive the winds from single Doppler radar under some assumptions, as the wind patterns are generally uniform or axisymmetric rotational (Cha and Bell, 2021). More extended techniques based on VTD and GBVTD have also been applied to increase the quality of derived wind data, and such techniques include Extended-GBVTD (EGBVTD, Liou et al., 2006) and generalized velocity track display (GVTD, Jou et al., 2008). However, winds usually present nonuniform patterns and fast-evolving characteristics in most mesoscale weather systems and microscale phenomena, and complete and detailed winds are still

68 difficult to resolve by these techniques. Most developed techniques are based on the contexts of

69 weaknesses from the above schemes on wind retrievals. Instead of a single Doppler radar,

70 multiple Doppler can retrieve better quality 3D winds with relativity fewer assumptions because

71 they provide sufficient radial velocity measurements and wind information with wider coverage

72 in the synthesis domain.

73 Cartesian Space Editing, Synthesis, and Display of Radar Fields under Interactive Control

74 (CEDRIC, Mohr and Miller, 1983) is a traditional package used to retrieve 3D winds by dual-

75 Doppler radar observations. This scheme usually determines the horizontal winds by using two

76 radars, and the vertical velocity can be obtained by variational adjustment with anelastic

77 continuity equation. Spline Analysis at Mesoscale Utilizing Radar and Aircraft Instrumentation

78 (SAMURAI) software is another way to retrieve 3D winds (Bell et al., 2012); this scheme is a

79 kind of variational data assimilation that adopts multiple radars. Recently, Tsai et al. (2018)

80 utilized the measurements of six Doppler radars to document precipitation and airflow structures

81 over complex terrain on the northeastern coast of South Korea via ~~WISSDOM (~~Wind Synthesis

82 System using Doppler Measurements [WISSDOM,~~).~~ Liou and Chang (2009)~~] is the first purposes~~

83 ~~of this algorithm~~. ~~Furthermore, they performed immersed boundary method (IBM, Tseng and~~

84 ~~Ferziger, 2003) in WISSDOM,~~ The~~and its~~ scientific studies and applications of WISSDOM were

85 well documented in Liou et al. (2012) and Liou et al. (2016)~~, respectively~~. In addition,

86 Immersed Boundary Method (IBM, Tseng and Ferziger, 2003) was applied in WISSDOM. Since

87 one of the advantages of WISSDOM is that it considers the orographic forcing on Cartesian

88 coordinates by applying the IBM, higher quality 3D winds can be derived well over terrain (Liou

89 et al., 2013, 2014, Lee et al., 2018).

90 Generally, radial velocity is measured by detecting the movement of precipitation particles

91 relative to the locations of Doppler radars; thus, there are no sufficient radial velocity

92 measurements under clear-air conditions. However, the winds in clear-air conditions usually play

93 an important role in the initiations of various weather systems and phenomena, such as downslope

94   winds, gap winds, and wildfires (Reed, 1931, Colle and Mass, 2000, Mass and Ovens, 2019, Lee

95   et al., 2020). Although surface stations, soundings, and wind profilers can measure winds under

96   clear-air conditions, relatively poor spatial coverage is still a problem for obtaining sufficient

97   wind information in certain local areas. Therefore, scanning Doppler lidars will be one approach

98   to obtain wind information under clear-air conditions. Päschke et al. (2015) assessed the quality

99   of wind derived by Doppler lidar with a wind profiler in a year trial, and the results showed good

100   agreement in wind speed (the error ranged between 0.5 and 0.7 m s^{-1}) and wind direction (the

101   error ranged between 5° and 10°). Bell et al. (2020) combined an intersecting range height

102   indicator (RHI) of six Doppler lidars to build "virtual towers" (such as wind profilers) to

103   investigate the airflow over complex terrain during the Perdigäo experiment. These virtual towers

104   can fill the gap in wind measurements above meteorological towers. The uncertainty of wind

105   fields is also reduced by adopting multiple Doppler lidars (Choukulkar et al., 2017), and a high

106   spatiotemporal resolution of derived wind is allowed to check small-scale rotors in mountainous

107   areas (Hill et al., 2010).

108   The original WISSDOM was designed to retrieve 3D winds based on Doppler radar

109   observations and background inputs combined with conventional observations and modeling.

110   However, the original WISSDOM only provided 3D winds under precipitation conditions. It does

111   not work well under clear-air conditions because Doppler radar cannot easily detect radial

112   velocity without precipitation particles. To obtain high-quality 3D winds under clear-air

113   conditions, the radial velocity observed from the scanning Doppler lidars can be used in the

114   modified WISSDOM. The results will allow us to investigate the initiations of precipitation

115   systems in advance of rainfall and snowfall, which is an essential benefit rather thanover Doppler

116   radar data in related research topics. Furthermore, the conventional observations and modeling

117   datasets were used as isolated constraints in the modified WISSDOM synthesis scheme. One of

118   the benefits of the isolated constraints is that it is easy to synthesize any kind of wind information

119   obtained from available datasets and give suitable weighting coefficients with different

120   constraints when they are processing the minimization in the cost function. Thus, more reliable

121   3D winds in clear-air conditions were well derived from this modified WISSDOM synthesis

122   scheme.

123   The objective of this study is to modify the WISSDOM synthesis scheme based on the

124   original version to be a more flexible and useful scheme by adding any number of Doppler lidars

125   and conventional observations as well as modeling datasets. This modified WISSDOM will allow

126   us to obtain an exceedingly high spatial resolution of 3D winds (50 m was set in this study) under

127   clear-air conditions. A resolution of 50 m was chosen in this study, as the Doppler lidars'

128   respective horizontal resolution averages 40-60 m. A variety of adequate datasets were collected

129   during a strong wind event in the winter season during an intensive field experiment ICE-POP

130   2018 (International Collaborative Experiments for Pyeongchang 2018 Olympic and Paralympic

131   winter games). In summary, the main goal of this study is to use Doppler lidar observations to

132   retrieve high-resolution 3D winds over terrain with clear-air conditions via WISSDOM. In this

133   study, detailed principles of the modified WISSDOM and data implementation are elucidated in

134   the following sections. In addition, the modified WISSDOM was ~~performed~~ used to retrieve 3D

135   winds over complex terrain under clear-air conditions in a strong wind event. The reliability of

136   the derived 3D winds was also evaluated and discussed with respect to conventional observations.

137   **2. Methodology**

138   **2.1 Original version of WISSDOM (WInd Synthesis System using DOppler Measurements)**

139   WISSDOM is a mathematically variational-based scheme to minimize the cost function, and

140   various wind-related observations can be used as one of the constraints in the cost function. The

141   3D winds were derived by variationally adjusted solutions to satisfy the constraints in the cost

142   function; thus, this is a gradient decent technique to converge toward a solution. The original

143   version of WISSDOM ~~performed~~ utilized five constraints, including radar observations (i.e.,

144   reflectivity and radial velocity), background (combined with automatic weather stations,

145   sounding, model or reanalysis data), continuity equation, vorticity equation, and Laplacian

146   smoothing (Liou and Chang 2009). Liou et al. (2012) applied the IBM in WISSDOM to consider

147   the topographic effect on the nonflat surfaces. One of the advantages of IBM is providing realistic

148   topographic forcing without changing the Cartesian coordinate system into a terrain-following

149   coordinate system. More scientific documentation associated with the interactions between

150   terrain, precipitation, and winds in different areas can be found in Liou et al. (2016) for Taiwan

151   and in Tsai et al. (2018) for South Korea. The cost function can be expressed as

$$J = \sum_{M=1}^{5} J_M, \tag{1}$$

153   where J_M is the different constraints. J_1 is the constraint related to the geometric relation

154   between radar radial Doppler velocity observations (V_r) and derived one from true winds ($\mathbf{V}_t =$

155      $u_t\mathbf{i} + v_t\mathbf{j} + w_t\mathbf{k}$) in Cartesian coordinates [eq. (2)]. Note that ~~the~~ $\mathbf{V}_t$ is~~will be~~ first

156   ~~guessed~~estimated based ~~, resulting from~~on the background of the sounding observations used

157   in this study. In the absence of background observations, the first guess of $\mathbf{V}_t$ is set to 0.

$$J_1 = \sum_{t=1}^{2} \sum_{x,y,z} \sum_{i=1}^{N} \alpha_{1,i} \left(T_{1,i,t}\right)^2. \tag{2}$$

159   Since WISSDOM is a scheme that uses the 4DVAR approach, the variations between different

160   time steps (t) should be considered, and two time steps of radar observations were collected in

161   this constraint and all following constraints. The x, y, z indicates the locations of a given grid

162   point in the synthesis domain, and i could be any number (N) of radars (at least 1). ~~–~~The α_1 is

163   the weighting coefficient of J_1 (α_2 is the weighting coefficient of J_2 and so on). $T_{1,i,t}$ in eq.

164   (2) is defined as eq. (3):

$$T_{1,i,t} = (V_r)_{i,t} - \frac{\left(x - P_x^i\right)}{r_i} u_t - \frac{\left(y - P_y^i\right)}{r_i} v_t - \frac{\left(z - P_z^i\right)}{r_i} \left(w_t - W_{T,t}\right), \tag{3}$$

166   $(V_r)_{i,t}$ is the radial velocity observed by the radar (i) at time step (t), P_x^i, P_y^i and P_z^i depict the

167   coordinate of radar i. The u_t, v_t and w_t $(W_{T,t})$ denote the 3D winds (terminal velocity of

168   precipitation particles) at given grid points at the time step t ; and $r_i =$

169   $\sqrt{(x - P_x^i)^2 + (y - P_y^i)^2 + (z - P_z^i)^2}$.

170   The second constraint is the difference between the background $(\mathbf{V}_{B,t})$ and true (derived)

171   wind field $(\mathbf{V}_t = u_t\mathbf{i} + v_t\mathbf{j} + w_t\mathbf{k})$, which is defined as

$$J_2 = \sum_{t=1}^{2} \sum_{x,y,z} \alpha_2 (\mathbf{V}_t - \mathbf{V}_{B,t})^2. \tag{4}$$

172

173   There were several options to obtain background in the original version of WISSDOM. The most

174   popular background resource involves using sounding observations; however, it can only provide

175   homogeneous wind information for each level in WISSDOM with relatively coarse temporal

176   resolution (3- to 12-hour intervals). The other option is combining sounding observations with

177   AWS (automatic weather station) observations. Although the AWS provided wind information

178   with better temporal resolution (1-min), the data were only observed at the surface layer with

179   semirandom distributions. The last option is to combine sounding, AWS, modeling or reanalysis

180   datasets. However, various datasets with different spatiotemporal resolutions are not favorable

181   for appropriate interpolation of given grid points of WISSDOM synthesis, and the accuracy and

182   reliability of the background may have been significantly affected by such a variety of datasets.

183   Thus, these different observed or model data should be treated differently to minimize

184   uncertainties and improve accuracy. Therefore, one of the improvements in the modified

185   WISSDOM is that these inputs were individually separated into independent constraints with

186   flexible interpolation methods. In addition, individual constraints were calculated in~~considered~~

187   ~~the~~ two time steps if the temporal resolution of the inputs was ~~equal to or~~ high enough. ~~er than~~

188   ~~the time interval of the WISSDOM outputs. Note that t~~The sounding observations are still a

189   necessary dataset because the air density and temperature profile were used to identify the height

190 of the melting level. In this study, sounding winds were adopted to represent the background for

191 each level and a constraint at the same time; nevertheless, the AWS and reanalysis dataset are

192 independent constraints in the modified WISSDOM (details are provided in the following

193 section).

194   The third, fourth and fifth constraints in the cost function are the anelastic continuity

195 equation, vertical vorticity equation and Laplacian smoothing filter, respectively. Equations (5),

196 (6) and (7) are denoted as follows:

$$J_3 = \sum_{t=1}^{2} \sum_{x,y,z} \alpha_3 \left[\frac{\partial(\rho_0 u_t)}{\partial x} + \frac{\partial(\rho_0 v_t)}{\partial y} + \frac{\partial(\rho_0 w_t)}{\partial z} \right]^2, \tag{5}$$

$$J_4 = \sum_{x,y,z} \alpha_4 \left\{ \frac{\partial \zeta}{\partial t} + \left[u \frac{\partial \zeta}{\partial x} + v \frac{\partial \zeta}{\partial y} + w \frac{\partial \zeta}{\partial z} + (\zeta + f)\left(\frac{\partial u}{\partial x} + \frac{\partial v}{\partial y} \right) + \left(\frac{\partial w}{\partial x}\frac{\partial v}{\partial y} - \frac{\partial w}{\partial y}\frac{\partial u}{\partial z} \right) \right] \right\}^2, \tag{6}$$

$$J_5 = \sum_{t=1}^{2} \sum_{x,y,z} \alpha_5 [\nabla^2 (u_t + v_t + w_t)]^2. \tag{7}$$

200 ρ_0 in eq. (5) is the air density, and $\zeta = \partial v/\partial x - \partial u/\partial y$ in eq. (6). The main advantage is that

201 using vertical vorticity can provide further improvement in winds and thermodynamic retrievals

202 from a method named as Terrain-Permitting Thermodynamic Retrieval Scheme (TPTRS, Liou et

203 al. 2019).

2.2 The modified WISSDOM

205   In addition to the five constraints in the original version, the modified WISSDOM synthesis

206 scheme includes three more constraints in the cost function. Thus, the cost function in the

207 modified WISSDOM was written as

$$J = \sum_{M=1}^{8} J_M. \tag{8}$$

209       $J_1 \sim J_5$ in (8) are the same constraints corresponding to equations (2)-(7). The main purpose

210 of this study is to retrieve 3D winds under clear-air conditions in which observational data are

211 relatively rare. Instead of the radial velocity $(V_r)_{i,t}$ observed from Doppler radars in eq. (3) in

212 original version of WISSDOM, the radial velocity observed from Doppler lidars was adopted in

213 the modified WISSDOM synthesis. In addition, if there were no precipitation particles under

214 clear-air conditions, the terminal velocity of precipitation particles $(W_{T,t})$ was set to zero in eq.

215 (3) in the modified WISSDOM. In this study~~,~~ the time steps in WISSDOM ~~were~~ are set ~~by the~~

216 ~~synthesis time and~~ to 12 min~~, s~~ ~~before the synthesis time due~~corresponding to the temporal

217 resolution of the primary input lidar data ~~being 12 mins~~. ~~Notably, R~~relatively minor changes in

218 environmental conditions were assumed in WISSDOM due to the limitation on the coarse

219 temporal resolution from specific inputs. For example, the closest time step of a sounding

220 observation or LDAPS dataset was chosen regarding the synthesis time, and the time constrain

221 was set to be the same.

222   The sixth constraint is the difference between the derived wind fields and the sounding

223 observations ($\mathbf{V}_{S,t}$), as defined in (9):

224
$$J_6 = \sum_{t=1}^{2} \sum_{x,y,z} \alpha_6 \left(V_t - V_{S,t}\right)^2. \tag{9}$$

225 The sounding data in J_6 were interpolated to the given grid points near its tracks bearing on the

226 radius influence (RI) distance (the details are provided in Section 3.2.3). The main difference

227 between J_6 and J_2 is that the sounding data with various wind speeds and directions were used

228 as an observation for given 3D locations in J_6 instead of the constraint of homogeneous

229 background winds (i.e., uniform wind speed and direction) for each level in the studied domain

230 in J_2. An additional benefit of J_6 is that any number of sounding observations can be efficiently

231 adopted in the WISSDOM synthesis domain. The seventh constraint represents the discrepancy

232 between the true (derived) wind fields and AWS ($\mathbf{V}_{A,t}$), as expressed in (10):

233
$$J_7 = \sum_{t=1}^{2} \sum_{x,y,z} \alpha_7 \left(V_t - V_{A,t}\right)^2. \tag{10}$$

234 Finally, the eighth constraint measures the misfit between the derived winds and the local

235   reanalysis dataset ($\mathbf{V}_{L,t}$), as defined in (11):

$$J_8 = \sum_{t=1}^{2} \sum_{x,y,z} \alpha_8 \left(V_t - V_{L,t}\right)^2. \tag{11}$$

237   In this study, various observations and reanalysis datasets were utilized as constraints in the cost

238   function of WISSDOM. The most important dataset is the radial velocity observed from Doppler

239   lidars, which can measure wind information with high spatial resolution and good coverage from

240   near the surface up to higher layers in the test domain. Sounding and AWS can provide horizontal

241   winds for background or to be included in the constraints. The local reanalysis datasets were

242   obtained from the 3DVAR Local Data Assimilation and Prediction System (LDAPS) data

243   assimilation system from the Korea Meteorological Administration (KMA). Since these datasets

244   have different coordinate systems and various spatiotemporal resolutions, additional procedures

245   are required before the synthesis. Detailed descriptions of the procedures are described in the next

246   section.

247   The high-quality synthesized 3D wind field from radar observations has been applied in

248   several previous studies such as those by Liou and Chang (2009), Liou et al. (2012, 2013, 2014,

249   2016), and Lee et al. (2017). The advantages and details of the WISSDOM can be found in Tsai

250   et al. (2018). Although several studies have used Doppler radar in WISSDOM, this study is the

251   first time to apply Doppler lidar data in WISSDOM. This modified WISSDOM synthesis scheme

252   has also been applied in the analysis related to the mechanisms of orographically induced strong

253   wind on the northeastern coast of Korea (Tsai et al., 2022). In contrast to previous studies, this

254   study provides clear context, detailed procedures, reliability, and the limitations of the modified

255   WISSDOM.

256   **3. Data processing with a strong wind event**

257   **3.1 Basic information of WISSDOM synthesis**

258   A small domain near the northeastern coast of South Korea was selected to derive detailed

259   3D winds over complex terrain (in the black box in the inset map in Fig. 1) because relatively

260   dense and high-quality wind observations were only collected in this region during ICE-POP

261   2018. The size of the WISSDOM synthesis domain is 12×12 km^2 (up to 3 km MSL height) in

262   the horizontal (vertical) direction with 50 m grid spacing. Such high spatial resolution 3D winds

263   were synthesized every 1 hour in this test. ~~Note that t~~The output time steps are adjustable to be

264   finer (recommended limitation is 10 mins), but they are highly related to the temporal resolution

265   of various datasets and computing resources. Two scanning Doppler lidars are located near the

266   center of the domain: one is the equipped "WINDEX-2000" (the model's name from the

267   manufacturer) at the May Hills Supersite (MHS) site, and the other is the "Stream line-XR" at

268   the DaeGwallyeong regional Weather office (DGW) site. In addition to the operational AWS

269   (727 stations), additional surface observations (32 stations) are also involved in ICE-POP 2018

270   surrounding the MHS and DGW sites and the venues of the winter Olympic Games. The

271   soundings are launched at the DGW site every 3 hours during the research period. The LDAPS

272   also provided high spatial resolution of wind information in the test domain. The horizontal

273   distribution of all instruments and datasets used are shown in Fig. 1.

274
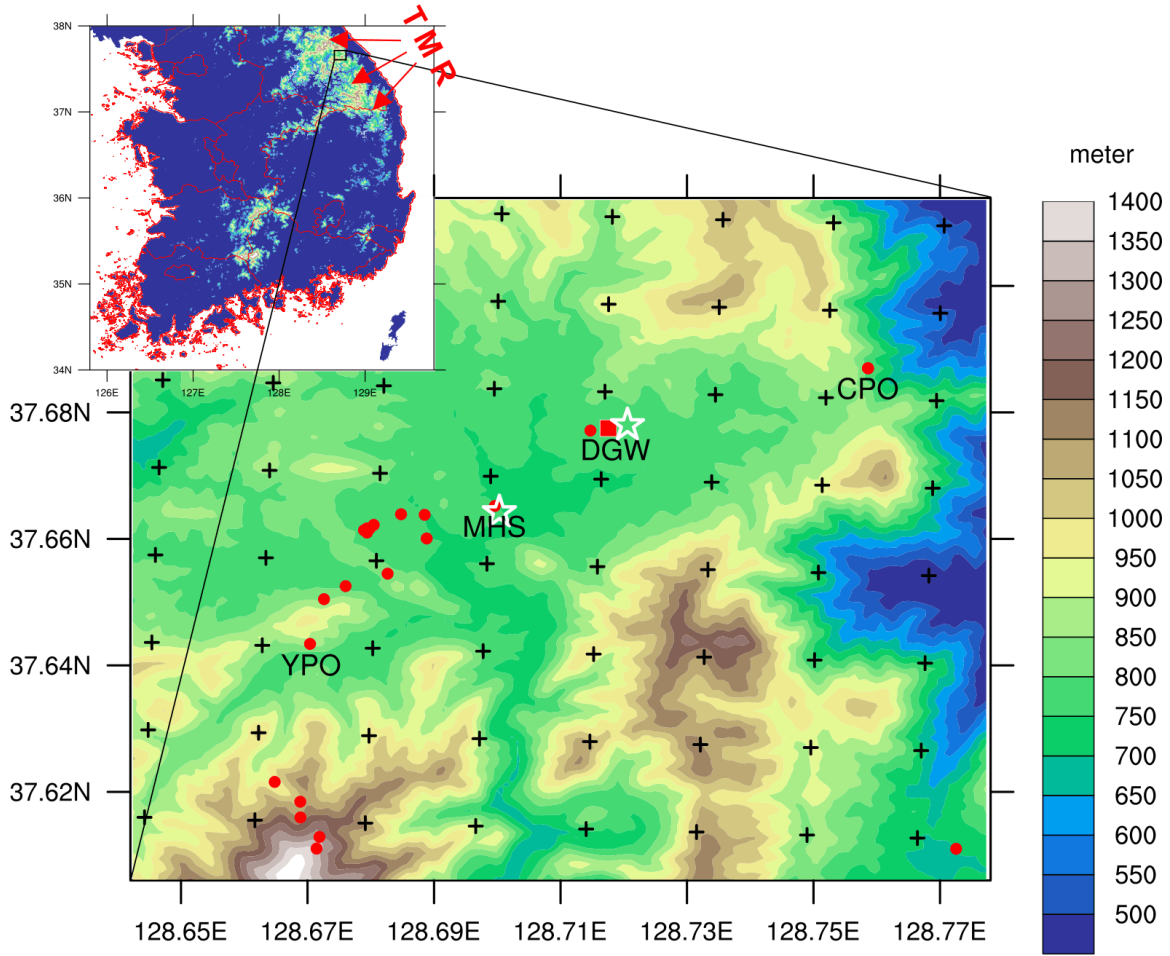
Figure 1. Horizontal distribution of instruments and datasets used in this study. A small box in the upper map indicates the WISSDOM synthesis domain. The Doppler lidars are marked by start symbols at the MHS and DGW sites. Red solid circles and square indicate the automatic weather station (AWS) and sounding, respectively. The black cross marks the data points of LDAPS. Topographic features and elevations are shown with the color shading in a color bar in the figure. The location of the Teabeak Mountain Range (TMR) is also marked.

3.2 Data implemented in WISSDOM synthesis

3.2.1 Scanning Doppler lidars

The radial velocity observed from two scanning Doppler lidars was utilized to retrieve 3D winds via WISSDOM synthesis. The original coordinate system of observed lidar data is not a Cartesian coordinate system but a spherical (or polar) coordinate system as a plan position indicator (PPI) and hemispheric range height indicator (HRHI) or the RHI. Although relatively dense and complete coverage of wind information (i.e., radial velocity of aerosols) were

287   sufficiently recorded by lidar observations, the collected data are usually not located directly on

288   the given grid points in the WISSDOM synthesis (i.e., Cartesian coordinate system). In this study,

289   the lidar data were interpreted simply from the lidar coordinate system to the Cartesian coordinate

290   system via bilinear interpolation.

291   The scanning strategy of the lidar at the DGW site includes five elevation angles for PPI (7°,

292   15°, 30°, 45°, and 80° before 10:00 UTC on 14 Feb. 2018 and 4°, 8°, 14°, 25°, and 80° after 10:00

293   UTC) and two HRHIs at azimuth angles of 51° and 330°. A full volume scan included all PPIs

294   and HRHIs every ~12 min. The maximum observed radius distance is ~13 km, and the grid

295   spacing is 40 m for each gate along the lidar beam. The scanning strategy of the lidar at the MHS

296   site involves seven elevation angles for PPI (5°, 7°, 10°, 15°, 30°, 45°, and 80°) and one HRHI

297   at an azimuth angle of 0°. A full volume scan included all PPIs and RHIs every ~12 min. The

298   maximum observed radius distance was ~8 km, and the grid spacing was 60 m. The vertical

299   distribution of lidar data in the test domain is shown as blue lines in Fig. 2a.

300   **3.2.2 Automatic weather station (AWS)**

301   Most of the AWS are not exactly located on the given grid points of the Cartesian coordinate

302   system. Objective analysis (Cressman, 1959) is a popular way to correct semirandom and

303   inhomogeneous meteorological fields into regular grid points. ~~Notably, that the wind directions~~

304   ~~and speed must be the first project with the values along the u- and v components, and then,~~

305   ~~their values must be interpolated individually to the given grids.~~ This study adopted objective

306   analysis for the AWS observations with adjustable RI distances between 100 m and 2000 m. After

307   this first step, the observational data can reasonably interpolate to the given grid points

308   horizontally. Furthermore, an additional step is required to put these interpolated data into the

309   given grid points at different vertical levels because the AWS are located at different elevations

310   in the test domain. In the traditional way of original WISSDOM, the interpolated data are moved

311   to the closest level with the shortest distance just above the AWS site. However, the interpolated

312   data are NOT moved to the closest level if the shortest distances are large like more than half

313   (50%) of grid spacing. Nevertheless, to include more data from the AWS observations

314   appropriately, adjusted distances between the AWS sites and given grid points at different vertical

315   levels were necessarily considered. These adjusted distances can be named as vertical extension

316   (VE) here, and there are two options of 50% and 90% in the tests of this study, which correspond

317   to 25 m and 45 m extensions between each grid (in case of the grid spacing is 50 m), respectively.

318   An example demonstrated how to implement the interpolated data to the given grid points by

319   adjustable VE after step one (Fig. 2b).

320   In Fig. 2b, the interpolated data do not need to move to a given grid point (as an example, at

321   the 800 m level here) if the elevation of the AWS is equal to the height of a given grid point as

322   point A. When the AWS is located higher than a given grid point (as point B in Fig. 2b) and does

323   not reach the lower boundary of VE (50%) from the upper given grid point (i.e., at the 850 m

324   level), this interpolated data will be removed and wasted. In contrast, when the interpolated data

325   are located just below the given grid point with 50% VE, it will be achieved in the WISSDOM

326   synthesis at the 800 m level (point C in Fig. 2b). The interpolated data of point D have a similar

327   situation to point B; however, it will be achieved at the 800 m level because a higher VE (90%)

328   was applied here. Since the locations of the AWS are semirandom with relatively sparse or

329   concentrated distributions, the optimal RI and adjustable VE make it possible to include more

330   AWS observations in the WISSDOM synthesis.
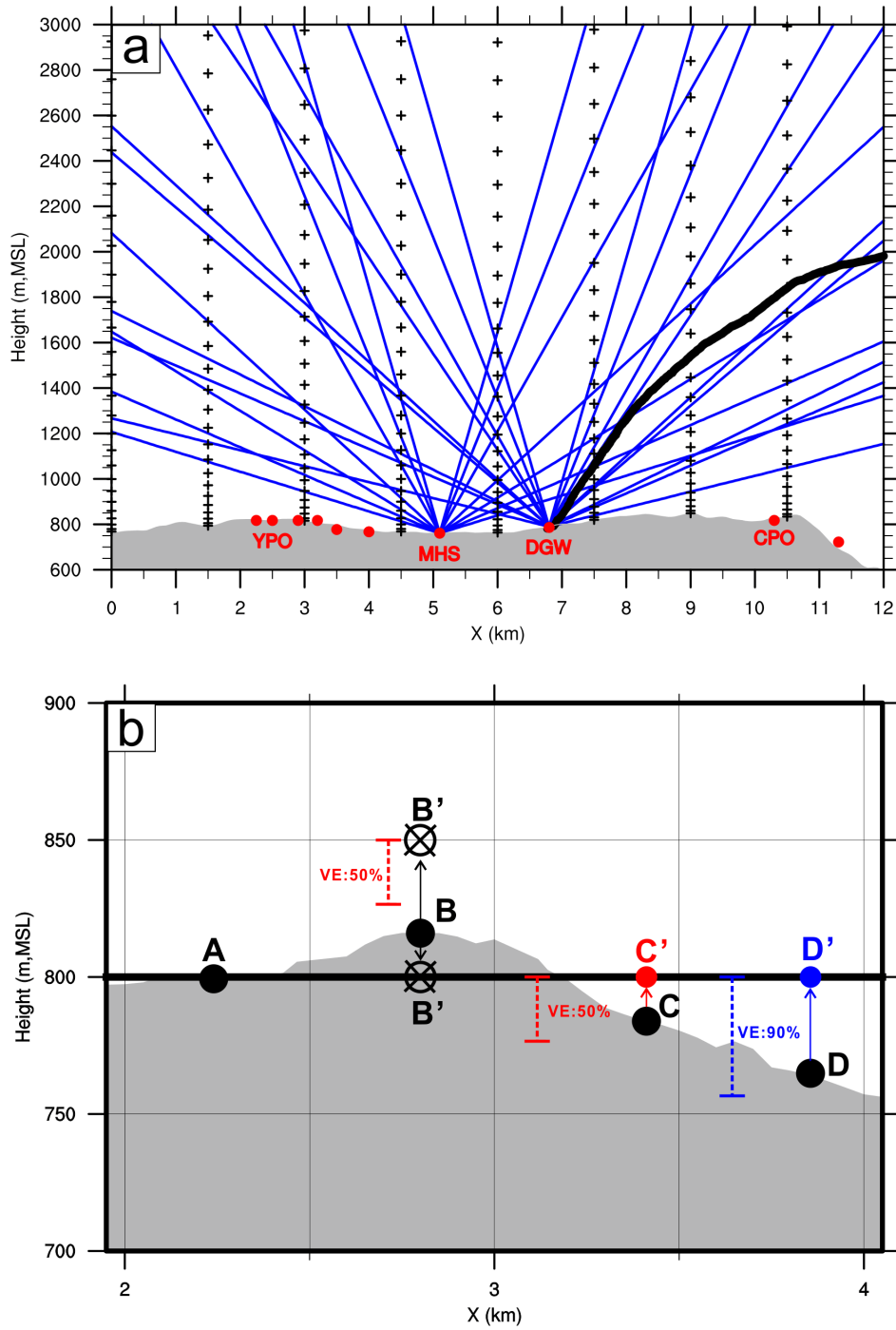
Figure 2. (a) Schematic diagram of the vertical distribution of adopted lidar datasets. Blue lines indicate the lidar data observed at the DGW and MHS sites with different elevation angles. The AWS are located on the ground and are marked by solid red circles. An example of a sounding track launched from the DGW site in one time step (06:00 UTC on 14 Feb. 2018) is plotted as a thick black line. The black cross marks indicate the vertical distribution of the LDAPS dataset. (b) Schematic diagram for data implementation with various locations of the AWS and different percentages of VE (vertical extension) from given grid points at the 800 m MSL level (thick black line). The gray shading on the bottom represents the topography.

3.2.3 Sounding

340   During ICE-POP 2018, the soundings are launched at the DGW site every 3 hours (from

341   00Z). Vertical profiles of air pressure, temperature, humidity, wind speed and directions were

342   recorded every second (i.e., ~3 m vertical spatial resolution) associated with the rising sensor.

343   The sounding sensor drifted when rising, and an example of its track in one time step is shown

344   as a thick black line in Fig. 2a. In this example, the sounding movement was mostly affected by

345   westerly winds, and it measured the meteorological parameters in any location along the track in

346   the test domain. The coordinate system of sounding data is quite similar to the distribution of

347   AWS measurements, and the observations are not located right on the given grid points of the

348   WISSDOM synthesis.

349   Similar to the AWS data, the sounding data also underwent objective analysis with an

350   adjustable RI distance for the wind measurements in the first step. Then, the interpolated data

351   were switched to given grid points for each vertical level by the different VE in the WISSDOM

352   synthesis.

353   **3.2.4 Reanalysis dataset: LDAPS**

354   The local reanalysis dataset LDAPS was generated by the KMA. This dataset provides u-

355   and v-component winds every 3 hours, and the horizontal spatial resolution is ~1.5 km with the

356   grid type in Lambert Conformal (as black cross marks in Fig. 1). The data revealed denser

357   distributions near the surface and sparse distributions at higher levels (see Fig. 2a). The initiations

358   of wind variables in the LDAPS were assimilated with many observational platforms, including

359   radar, AWS, satellite and sounding data. Thus, the relatively high reliability of this dataset could

360   be expected. In addition, such datasets have also significantly improved the forecast ability in

361   small-scale weather phenomena over complex terrain in Korea (Kim et al., 2019, Choi et al.,

362   2020, Kim et al., 2020).

363   The LDAPS data are not located directly on the given grid points of the WISSDOM synthesis

364   system. Unlike the distribution of AWS and sounding observations, LDAPS has dense and good

365 coverage in the test domain. The Cartesian coordinate system is the most efficient method and

366 the best system for partial differential equations (Armijo, 1969), and it is also used in the cost

367 function of WISSDOM (Liou and Chang, 2009). In this study, the horizontal and vertical

368 resolutions of given grid points were primarily determined by the characteristics of lidar data.

369 Therefore, similar to lidar observations, the LDAPS data were also interpolated to the given grid

370 points on the Cartesian coordinate system via the bilinear interpolation method.

371 **3.3 Overview of the selected strong wind event**

372   A strong wind event was selected to evaluate the performance of this modified WISSDOM

373 synthesis scheme. In this strong wind event, the evolution of surface wind patterns on the Korean

374 Peninsula was mainly dominated by a moving LPS which is one type of strong downslope winds

375 (Park et al, 2022, Tsai et al., 2022). The LPS moved out from China and penetrated the northern

376 part of the Korean Peninsula through the Yellow Sea beginning at approximately 12:00 UTC on

377 13 February 2018. Consequently, a relatively strong surface wind speed (exceeding ~17 m s^{-1})

378 was observed when the LPS was located near the northeastern coast of the Korean Peninsula

379 (~130°E, 40°N) at 00:00 UTC on 14 February 2018 (Fig. 3). Then, the surface wind speed became

380 weak when the LPS moved away from South Korea after 00:00 UTC on 15 February 2018 (not

381 shown); the details of the synoptic conditions can be found in Tsai et al. (2022).

382
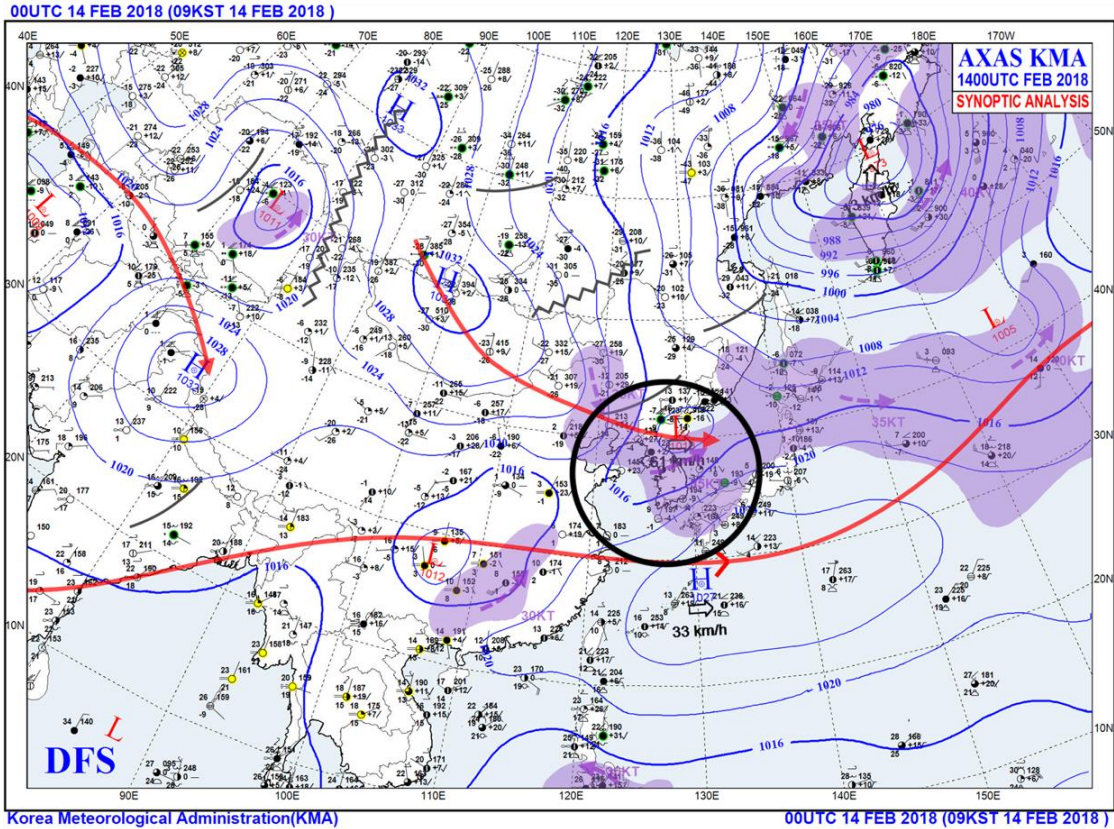
383   Figure 3. Synoptic surface chart from the Korea Meteorological Administration (KMA) at 00:00 UTC on 14 Feb.
384   2018. The locations of the Korean peninsula and the LPS has been marked by black circle.

385

386   This event is one of two strong wind events (i.e., daily maximum wind speeds larger than

387   10 m s^{-1} observed at the AWS sites along the northeastern coast of South Korea) in the past

388   decade based on the KMA historic record. Such a strong wind event may help us to examine the

389   potential maximum errors of the retrieved winds. Since persistent, strong westerly winds were

390   observed by the soundings and AWS from near the surface and upper layers over the TMR during

391   the event, the data coverages in the test domain were checked during a chosen time step (06:00

392   UTC on 14 February 2018). The percentage of data occupations for each dataset (after

393   interpolation) was checked, and the results are shown in Fig. 4. Note that the elevation of the

394   TMR is approximately 700 m MSL in the test domain. The lidars provided good coverage of

395   100% to 50% at the lower layers between 700 m and 800 m MSL. The coverage of lidars was

396   reduced significantly above 900 m MSL and remained at ~5% due to the scan strategy during the

397   Olympic games (more dense observations near the surface). The maximum coverage of the AWS

398   observations is ~40% at 800 m, and there was less coverage above this layer since relatively few

399   AWS are located in the higher mountains. Because only one sounding observation was utilized

400   in this domain, relatively few coverages were also depicted. The local reanalysis LDAPS can

401   provide complete coverage above 900 m MSL (exceeding 100%), albeit there was less coverage

402   in the lower layers due to terrain. The lidar, sounding, and AWS observations covered most areas

403   at lower levels but not higher levels; thus, the LDAPS compensated for most of the wind

404   information at the upper layers in the WISSDOM synthesis.
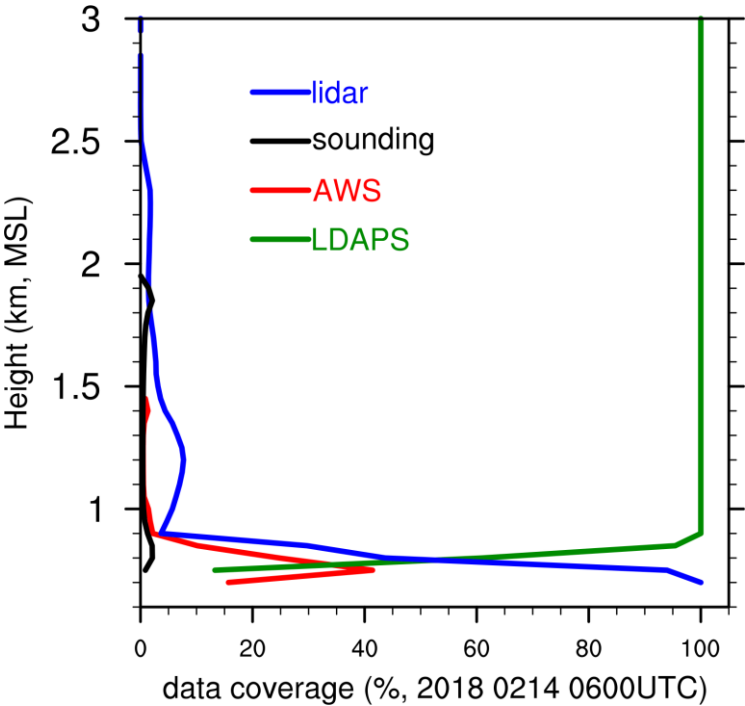
405

406   Figure 4. Data coverage (percentage, %) of the lidar (blue line), sounding (black line), AWS (red line) observations,

407   and LDAPS (green line) at 06:00 UTC on 14 Feb. 2018.

408   **4. Control run and the accuracy of WISSDOM**

409   **4.1 Control run**

410   Relatively reliable 3D winds were derived by a control run of the WISSDOM synthesis

411   because all available wind observations and local reanalysis datasets were appropriately acquired.

412   These datasets provided sufficient and complete wind information with a high percentage of

coverage in the test domain (cf. Fig. 4). Therefore, the retrieved winds from the control run can
be treated as the optimal results in WISSDOM. The control run was performed carefully with the
necessary procedures in data implementation before running the WISSDOM synthesis as follows.
The lidar and LDAPS datasets must perform bilinear interpolation to the given grid points in
WISSDOM, and the sounding and AWS observations must undergo objective analysis with the
appropriate RI distance and VE. The quantities of the weighting coefficients for each input dataset
followed the default setting from the original version of WISSDOM. The 3D winds were derived
during one time step at 06:00 UTC on 14 Feb. 2018 and compared with conventional
observations. ~~Note that t~~The best weighting coefficients have been determined by a series of
observation system simulation experiment (OSSE) type tests from Liou and Chang (2009). They
put more weight~~ing coefficients o~~in observations and ~~fewer~~ less o~~i~~n modeling inputs. Based on
the experiences and the default setting of weighting coefficients from their studies, the basic
setting of the control run was first decided. Consequently, sensitivity tests were performed to
better understand the possible ~~variances~~ variations associated with different weighting
coefficients when the lidar data were implemented. The basic setting of this control run is
summarized in Table 1.

Table 1   Basic setting of WISSDOM (control run)

Domain Range	Latitude: 37.606°N~37.713°N Longitude: 128.642°E~128.778°E
Domain Size	12 × 12 × 3 km (long × width × vertical)
Spatial Resolution	0.05 × 0.05 × 0.05 km (long × width × vertical)
Terrain Resolution	0.09 km
Coordinate System	Cartesian coordinate system
Background	Sounding (DGW)
Data Implementation	Doppler Lidars (MHS, DGW): bilinear interpolation AWS: objective analysis (RI*: 1 km, VE*: 90%) Sounding (DGW): objective analysis (RI: 1 km, VE: 90%) LDAPS: bilinear interpolation
Weighting Coefficient	Doppler Lidars (α_1): 10^6

(input datasets)	Background (α_2):10^2
	Sounding (α_6): 10^6
	AWS (α_7): 10^6
	LDAPS (α_8): 10^3

*RI: radius influence, VE: vertical extension

429   The results of 3D winds at 800 m MSL derived from the control run are shown in Figs. 5a,

430   c, and e. Topographic features comprised relatively lower elevations in the center of the test

431   domain, and there were weaker u-component winds (~7 m s^{-1}) near the AWS and MHS lidar sites

432   between 128.67°E and 128.71°E (Fig. 5a). In contrast, the u-component winds (~15 m s^{-1}) were

433   almost doubled near the DGW lidar site (between 128.71°E and 128.73°E). The vertical

434   structures of the u-component winds across these two lidars (i.e., along the black line in Fig. 5a)

435   are shown in Fig. 5b. The strength of the u-component winds rapidly increased from the surface

436   to the upper layers (from ~6 to 20 m s^{-1}), and uniform u-component winds with wavy pattern

437   were depicted above ~1 km MSL except for the stronger winds near the surface surrounding the

438   DGW site. There were relatively weak (strong) u-component winds surrounding the lidar at the

439   MHS (DGW) site near the surface. Relatively weak v-component winds were found

440   (approximately ±4 m s^{-1}) at 800 m MSL (Fig. 5c); thus, the horizontal wind directions were

441   mostly westerly winds during this time step. The v-component winds were obviously accelerated

442   in several local areas encompassing the terrain (near 128.71°E). The vertical structure of the v-

443   component winds (Fig. 5d) indicates that the v-component winds became stronger in the upper

444   layer. The wind directions were changed from westerly to southwesterly from the near surface

445   up to ~1.4 km MSL height. Updrafts were triggered on windward slopes when westerly winds

446   impinge the terrain or hills (Figs. 5e and 5f). Basically, the 3D winds derived from the WISSDOM

447   synthesis reveal reasonable patterns compared to synoptic environmental conditions (cf. Fig. 3);

448   the moving LPS accompanied stronger westerly winds.

449
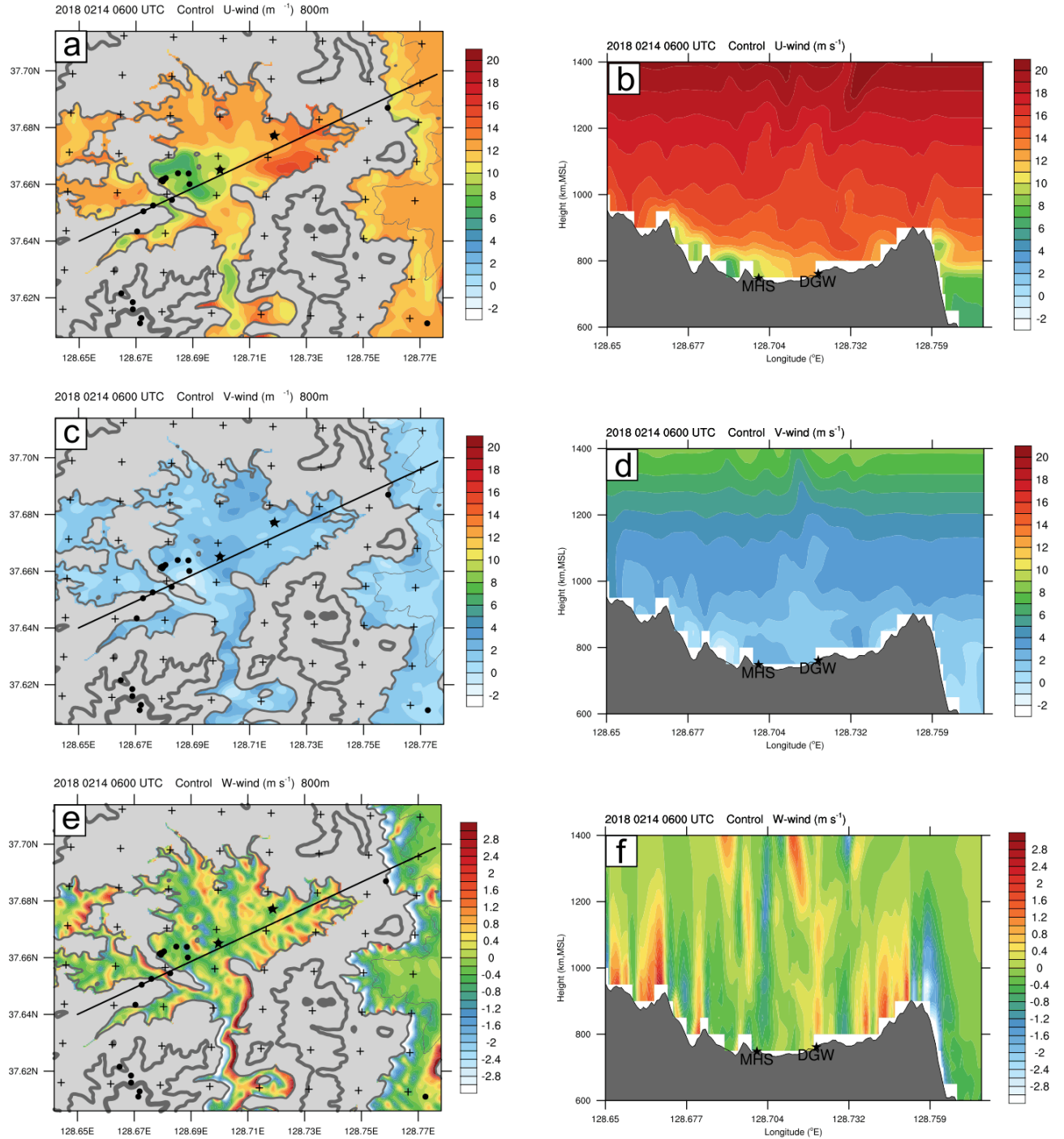
Figure 5. The 3D winds were derived from the control run by the WISSDOM synthesis at 06:00 UTC on 14 Feb. 2018. (a) The u-component winds (color, m s^{-1}) at 800 m MSL; the gray shading represents the terrain area, and the contours indicate different terrain heights of 600 m, 800 m and 1000 m MSL corresponding to thin to thick contours. The locations of lidars are marked with asterisks. (b) Vertical structures of u-component winds (color, m s^{-1}) along the black line in (a) The gray shading in the lower part of the figure indicates the height of the terrain. (c) and (d) are the same as (a) and (b) but for the v-component winds. (e) and (f) are the same as (a) and (b) but for the w-component winds.

4.2 Intercomparison between derived winds and observations

Detailed analyses were performed in this section to quantitatively evaluate the accuracy of the optimally derived 3D winds from the WISSDOM synthesis. Two kinds of instruments were available in the test domain to detect the relatively realistic winds: sounding and lidar quasi-vertical profiles (QVP, Ryzhkov et al., 2016). The QVP of horizontal and vertical winds were retrieved based on the ~~so-called~~ velocity-azimuth display (VAD) technique (Browning and Wexler, 1968, Gao et al., 2004). We regressed the Fourier coefficients of the Doppler velocities of the 80° PPI under the linear horizontal wind assumption and obtained the horizontal wind profile. The vertical (i.e., w-component) wind was retrieved under the assumptions of constant vertical wind, zero terminal velocity of aerosol particles, and no horizontal divergence [see Kim et al. (2022) for details on the wind retrieval]. The accuracy of the retrieved wind profile is suitable for the WISSDOM wind evaluation, given the low root mean square deviation (RMSD) of < 2.5 m s^{-1} and high correlation coefficient of > 0.94 of horizontal wind speed as shown in the comparison against 487 rawinsondes (Kim et al., 2022). The horizontal winds observed from the soundings and the u-, v-, and w-component winds of the lidar QVP at the DGW site were utilized to represent the observations.

A complete analysis of the intercomparison between the WISSDOM synthesis and observations is presented in the following subsections. Because the verification observations are being used in the WISSDOM synthesis, the results of the control run are not verified independently; nevertheless, detailed discussions regarding the results of the sensitivity tests for the observations are presented in Section 5.

4.2.1 Sounding

The discrepancies in horizontal winds derived from WISSDOM and the sounding observations for the entire research period (from 12:00 UTC on 13 to 12:00 UTC on 14 February

481   2018) were analyzed. Fig. 6 shows the scatter plots of the u- and v-component winds on the

482   locations following the tracks of sounding launched from the DGW site. Most of the u-component

483   winds derived from WISSDOM are in good agreement with the sounding observations, and the

484   wind speed is increased with the height from approximately 10 to 40 m s^{-1}. Slight underestimation

485   of retrieved u-component winds can be found at the layers of 1.5~2 km MSL (Fig. 6a). In contrast,

486   most of the v-component winds were weak (smaller than 15 m s^{-1}) at all layers, because the

487   environmental winds were more like westerlies during the research period. There were also

488   slightly overestimated v-component winds derived from WISSDOM at the layers of 1.5~2 km

489   MSL (Fig. 6b). The possible reason why the overestimated winds occurred above ~1.5 km MSL

490   is that lidar data had relatively less coverages at higher layers (cf. Fig. 4).

491
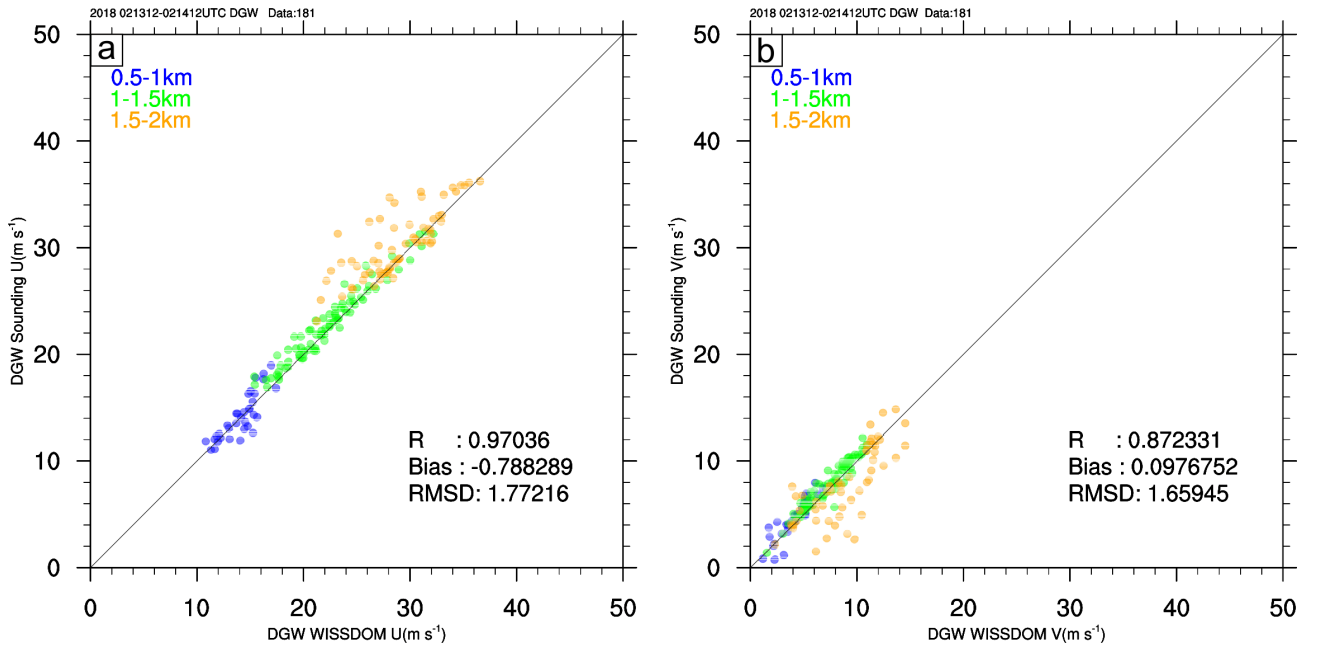
Figure. 6. Scatter plots of (a) u-component winds between the WISSDOM synthesis (x-axis) and sounding
      observations (y-axis) above the DGW site during the research period. The colors indicate different layers, and
      the numbers of data points, correlation coefficients, average biases and root mean square deviations are also
      shown in the figure. (b) The same as (a) but for v-component winds.

496   Overall, the u-component winds show a high correlation coefficient (exceeding 0.97), low

497   average bias (−0.78 m s^{-1}), and the RMSD of 1.77 m s^{-1}. The correlation coefficient of the v-

498   component is also high (0.87), the average bias is 0.09 m s^{-1}, and the RMSD is 1.65 m s^{-1}.

499
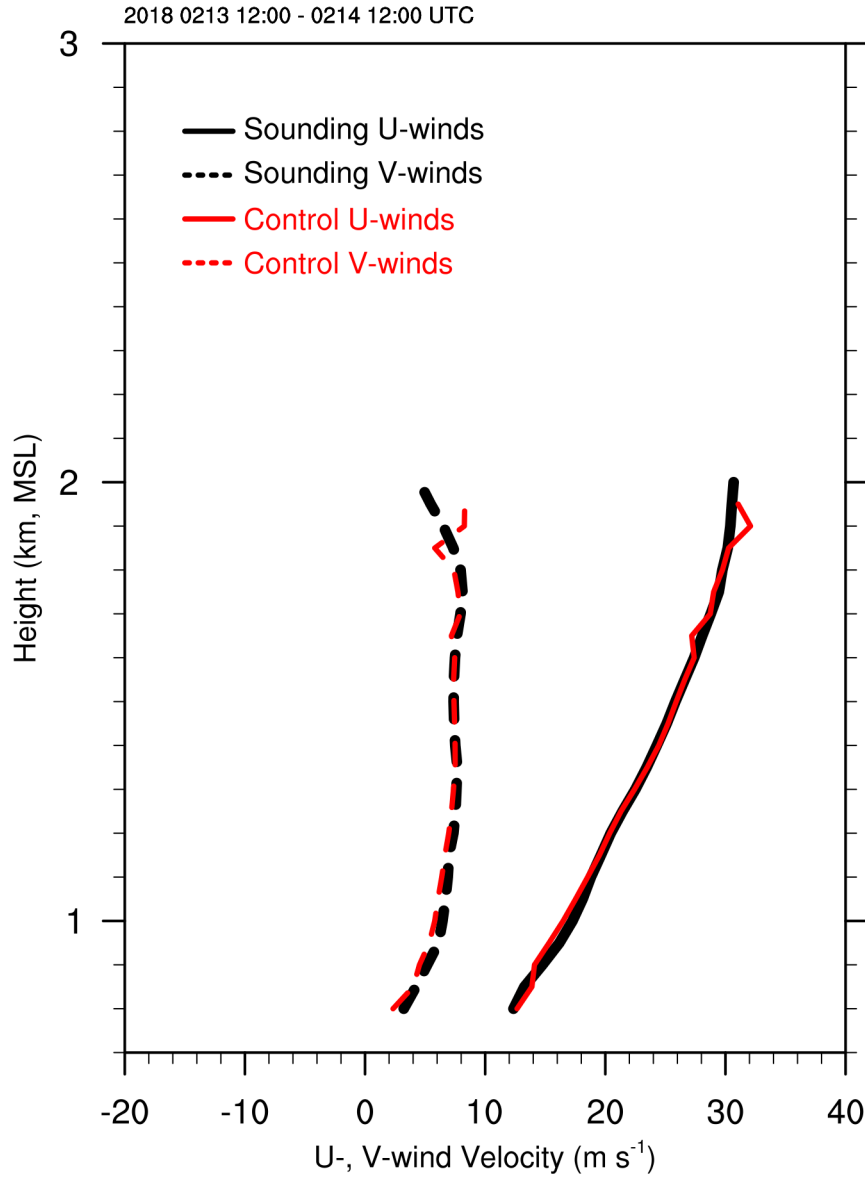
Figure 7. Vertical wind profiles of average horizontal winds derived from the WISSDOM synthesis (red lines and vectors) and sounding observations (black lines and vectors) above the DGW site from 12:00 UTC on 13 to 12:00 UTC on 14 Feb. 2018. Solid lines indicate u-component winds (m s^{-1}), and dashed lines indicate v-component winds (m s^{-1}).

The vertical profiles of the averaged u- and v-component winds for the period of 12:00 UTC on 13 to 12:00 UTC on 14 Feb. 2018 is shown in Fig. 7 for the WISSDOM synthesis (red) and sounding observations (black) launched from the DGW site. The average profiles agree well except for the height above 1.5 km MSL, slight discrepancies of u- and v-component winds (< 1 m s^{-1}). Their statistical errors during the entire research period were quantified by the box plot shown in Fig. 8.

510   The maximum difference in wind directions between the WISSDOM synthesis and sounding

511 observations is small at all layers. Only relatively larger IQR ~~(between ~ −5 and 5 degrees)~~ and

512 ~~larger~~ median values ~~(between ~0 and 5)~~ can only be found at the lowest level. The interquartile

513 range (IQR) and median values of the wind direction differences are smaller (between ~0 and 2.5

514 degrees) during the entire research period (Fig. 8a). Basically, the IQR and median values of the

515 wind direction differences are close to 0 degrees above 1 km MSL. Fig. 8b shows the difference

516 in wind speed between the WISSDOM synthesis and sounding observations. The differences of

517 wind speed derived from WISSDOM ~~was~~ were slightly underestimated in the layers between

518 ~0.85 and 1.3 km MSL. The median values of the wind speed differences were between −1 and

519 0.5 m s^{-1}, and the IQR of wind speed differences ~~was~~ were between −2 and 0.5 m s^{-1}. Above 1.3

520 km MSL, the differences in wind speed ~~are~~ were small as their median values are close to 0 m

521 s^{-1}.

522

523
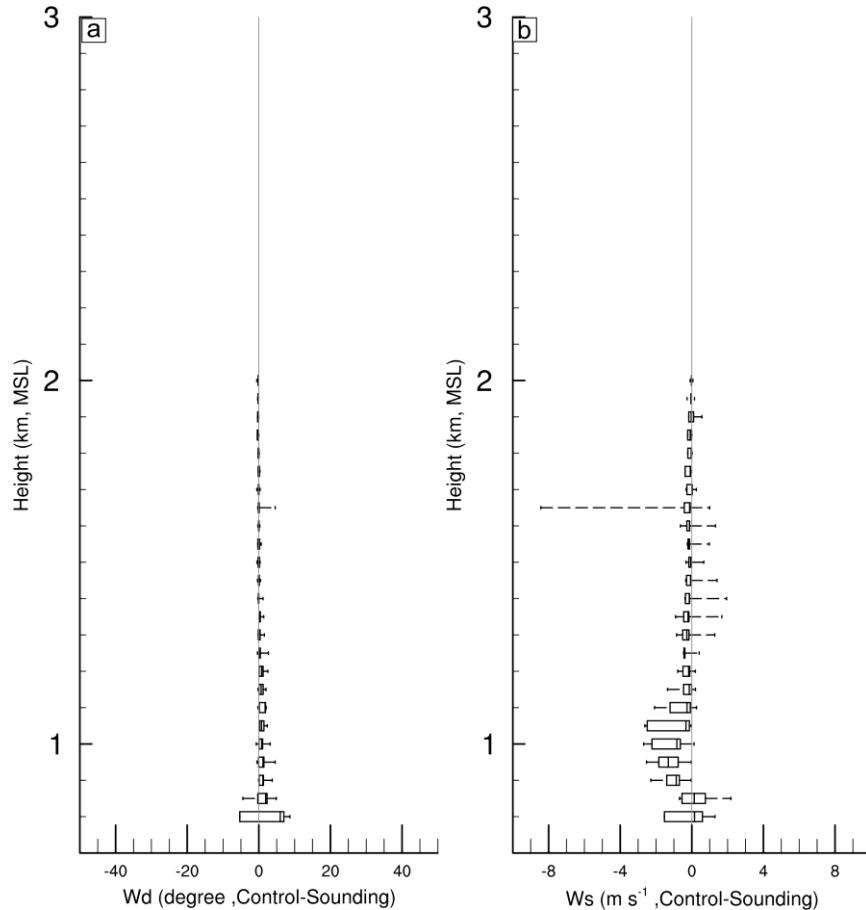
524 Figure 8. The box plot of average (a) wind direction discrepancies between the WISSDOM synthesis and sounding
525   observations above the DGW site during the research period. (b) Same as (a) but for the wind speed.

4.2.3 Lidar QVP

527   The lidar QVP is another observational reference used to evaluate the performance of derived

528 winds from the WISSDOM synthesis. The scatter plots of the horizontal winds derived from

529 WISSDOM and lidar QVP at the DGW site are shown in Fig. 9. The strength of the u-component

530 winds increases with height in the range between approximately 10 m s^{-1} and 40 m s^{-1} from the

531 surface up to ~2.5 km MSL (Fig. 9a). Although the results show a relatively high correlation

532 coefficient (0.84) for the u-component winds from lower to higher layers in the entire research

533 period, the degree of scatter is larger than that in Fig. 6a. The average bias and RMSD of the u-

534 component winds are 2.83 m s^{-1} and 3.69 m s^{-1}, respectively. The correlation coefficient of v-

535 component winds is lower (0.35) in association with low wind speed (<15 m s^{-1}) from the surface

536 to 2.5 km MSL (Fig. 9b), and it may possibly relate to less coverage from lidar QVP data at

537 higher layers. The average bias and RMSD of the v-component winds are 2.26 m s^{-1} and 2.92 m

538 s^{-1}, respectively. The results of these scatter plot analyses are summarized in Table 2. Basically,

539 the u-component winds have high correlations, relatively lower bias, and lower RMSD than the

540 v-component winds because the environmental winds are more westerly.

541
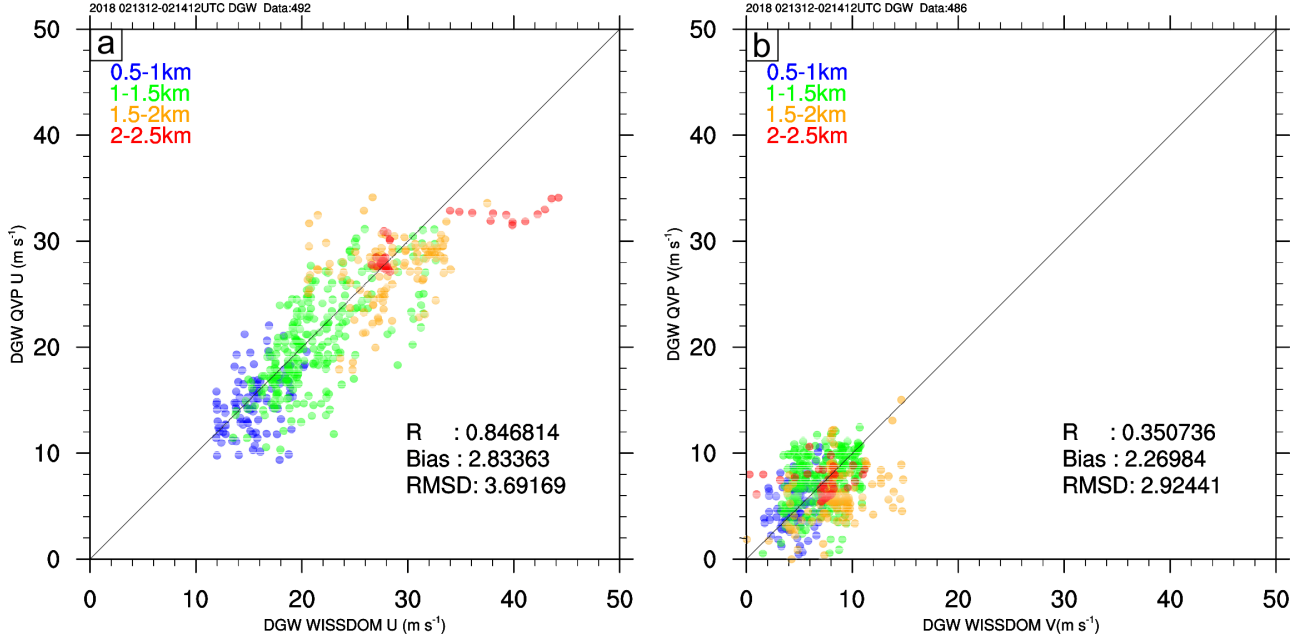
542 Figure 9. The same as Fig. 6 but for (a) u-component winds between the WISSDOM synthesis (x-axis) and lidar

543   QVP (y-axis). (b) The same as (a) but for v-component winds.

544

Table 2  Summary of the intercomparisons between WISSDOM and observations

		Correlation coefficient	Average bias (m s^{-1})	RMSD (m s^{-1})
WISSDOM-sounding	u-component	0.97	-0.78	1.77
	v-component	0.87	0.09	1.65
WISSDOM-lidar QVP	u-component	0.84	2.83	3.69
	v-component	0.35	2.26	2.92

545    Compared to the sounding observations, additional w-component winds are available in

546 lidar QVP, which allows us to check their discrepancies in 3D winds. However, most of the

547 vertical velocity observations were quite weak (approximately ±0.2 m s^{-1}) above the DGW site,

548 and relatively low reliability of the derived vertical velocity could be expected in this event.

549 Therefore, the average vertical profiles of 3D winds were utilized to qualitatively check the

550 discrepancies between WISSDOM synthesis and lidar QVP during the research period (Fig. 10).

551 The results show that the average u-component winds have relatively smaller discrepancies

552 (approximately <1 m s^{-1}) between the WISSDOM synthesis (marked as WISS-U in Fig. 10) and

553 lidar QVP (marked as QVP-U) below ~1.3 km MSL at the DGW site. In contrast, there were

554 larger discrepancies (approximately >2 m s^{-1}) between 1.3 km and 2 km MSL. The average v-

555 component winds derived from WISSDOM (marked as WISS-V) and lidar QVP (QVP-V) were

556 generally weak, and the ranges of WISS-V and QVP-V were between ~2 m s^{-1} and 8 m s^{-1}.

557 Generally, the vertical profiles of WISS-V were nearly overlain with QVP-V, and their

558 discrepancies existed in the height range 1.6~2.0 km MSL (maximum ~4 m s^{-1}). Smaller (larger)

559 discrepancies of w-component winds were significantly below (above) the height at ~1.3 km

560 MSL (maximum discrepancies ~0.6 m s^{-1} at 1.7 km MSL). Despite the larger discrepancies, the

561 similar patterns of W can also be shown. In summary, the discrepancies in the 3D winds between

562 the WISSDOM synthesis and lidar QVP were small in the lower layers and large in the higher

563 layers because the observational data from lidars and AWS provided good quality and sufficient

564 wind information at the lower layers but not in the higher layers (lower coverages of lidar data

565 above 1.3 km MSL, cf. Fig. 4).

566
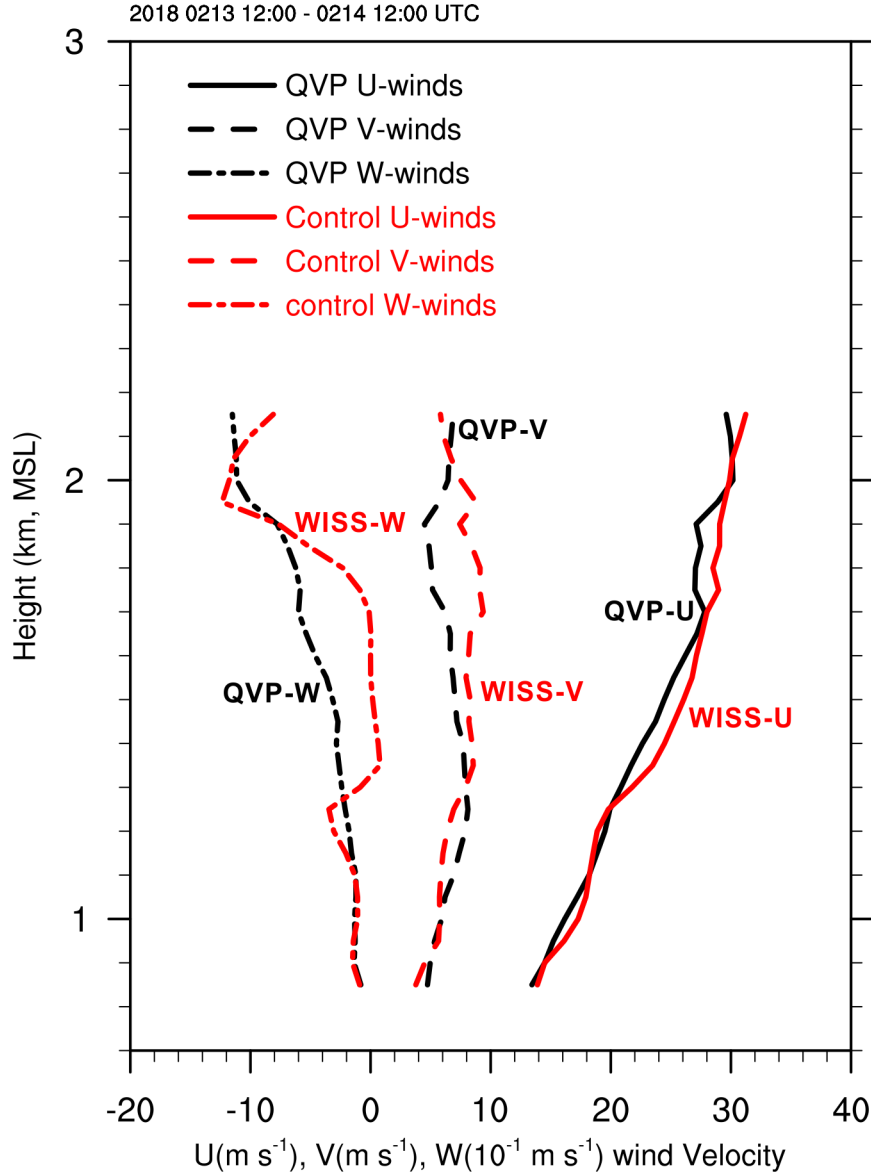
567 Figure 10. Vertical wind profiles of average 3D winds derived from the WISSDOM synthesis (red lines and vectors)
568   and lidar QVP (black lines and vectors) above the DGW site from 12:00 UTC on 13 to 12:00 UTC on 14 Feb.
569   2018. Solid lines indicate u-component winds (m s^{-1}), dashed lines indicate v-component winds (m s^{-1}), and
570   dash-dotted lines indicate w-component winds (1×10^1 m s^{-1}). The u-, v-, and w-component winds derived from
571   the WISSDOM synthesis (lidar QVP) were marked by WISS-U (QVP-U), WISS-V (QVP-V), and WISS-W
572   (QVP-W), respectively.

573   Fig. 11 shows the quantile distribution of statistical errors of wind direction, wind speed and

574 vertical velocity between the WISSDOM synthesis and lidar QVP during the research period.

575 The IQR of the wind direction is smaller (−5~5 degrees) in the layers from 0.85 km to 1.5 km

576 MSL and turns to approximately −10~0 degrees above 1.5 km MSL. The median values of wind

577 direction are smaller −5~5 degrees) from near the surface to the upper layers (Fig. 11a). Fig. 11b

578 shows that the median values (IQR) of wind speed are approximately –1~1 m s^{-1} (–2~2 m s^{-1})

579 below 1.5 km MSL, and they all become larger with heights above 1.5 km MSL (between −1 and

580 3 m s^{-1} for median values and −4~4 m s^{-1} for the IQR). The statistical error of the vertical velocity

581 reveals that the IQR is −0.2~0.2 m s^{-1} (−0.8~0.8 m s^{-1}) below (above) 1.3 km MSL, and the

582 median values are 0~0.2 m s^{-1} −0.2~0.6 m s^{-1}) below (above) 1.3 km MSL. The results of

583 statistical errors are summarized in Table 3.

584

585
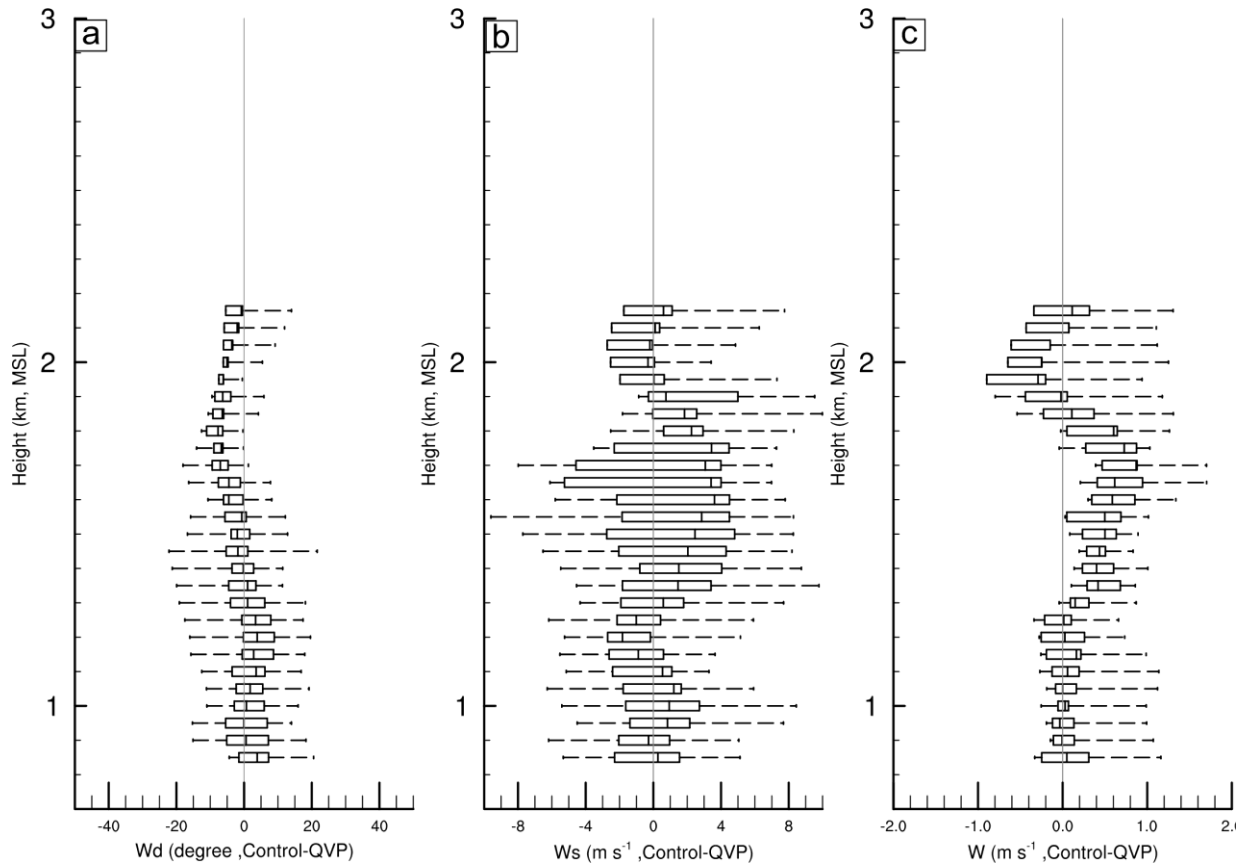
586 Figure 11. The box plot of average (a) wind direction discrepancies between the WISSDOM synthesis and sounding

587   observations above the DGW site during the research period. (b) Same as (a) but for the wind speed. (c) Same

588   as (a) but for the w-component winds.

589

Table 3   Summary of the statistical errors between WISSDOM and observations

		Interquartile range (IQR)	Median values
WISSDOM-sounding	wind direction	0~2.5 (deg.)	0~2.5 (deg.)
	wind speed	−2~0.5 (m s^{-1})	−1~0.5 (m s^{-1})

	wind direction	−10~5 (deg.)	−5~5 (deg.)
WISSDOM-lidar QVP	wind speed	-4~4 (m s^{-1})	−1~3 (m s^{-1})
	w-component winds	−0.8~0.8 (m s^{-1})	−0.2~0.6 (m s^{-1})

5. Sensitivity test with various datasets, data implementation and weighting coefficients

5.1 Impacts of various datasets (Experiment A)

In this section, the impacts of various datasets on data implemented in the WISSDOM synthesis were evaluated. In particular, the quantitative variances between each design, control run, sounding observations, and the QVP can be estimated. The basic setting of Experiment A took off several inputs from the WISSDOM control run (cf. Table 1) as four designs in Experiment A. The details of these four designs are summarized in Table 4 as the control run without the lidar observations (A-1), the control run without the AWS observations (A-2), the control run without the sounding observations (A-3) and the control run without the LDAPS data (A-4). The discrepancies of 3D winds were examined between the control run and each design in Experiment A. Since the environmental wind speed is nearly comprised of uniform westerlies in this event, the results only show the difference in u-component winds between control run and each design (A-1~A-4) in Fig. 12. An additional test was designed, where as only Doppler lidar data are used without other constraints from $J_6 \sim J_8$ (A-5) to evaluate the performances between the modified and original versions of WISSDOM.

Fig. 12a reveals the discrepancies in horizontal u-component winds at 800 m MSL as the A-1 is subtracted from the control run. This result reflects the impacts of lidar observations on the u-component winds in the WISSDOM synthesis. The most significant contributions from the lidar observations are the high wind speed existing near the DGW site in a relatively narrow

609   valley. The mechanisms of the accelerated wind speed due to the channeling effect in this local

610   area were verified by our previous study (Tsai et al. 2022). The lidar observations also contributed

611   to the high wind speed in another area near the western side of the MHS site (128.68°E, 37.66°N).

612   Based on the analysis in the vertical cross section of u-component winds in A-1 (Fig. 12b), the

613   lidar observations significantly affected the high wind speed only in the lower levels (below ~900

614   m MSL) but not in the higher levels. Lidar observations provided sufficient coverage only for

615   lower levels and not higher levels (cf. Fig. 4).

616

Table 4 Experiment setting (sensitivity testing)

Control run	Various datasets	Including Doppler lidars, AWS, Soundings, LDAPS
	Interpolation of AWS	RI: 1.0 km, VE: 90%
	Weighting Coefficient	Doppler Lidars (α_1): 10^6 Background (α_2):10^2 Sounding (α_6): 10^6 AWS (α_7): 10^6 LDAPS (α_8): 10^3
Experiment A	Various datasets	A-1 Excluding Doppler Lidars A-2 Excluding AWS A-3 Excluding Soundings A-4 Excluding LDAPS A-5 Only Doppler lidars
Experiment B	Interpolation of AWS	B-1 RI: 0.5 km, VE: 50% B-2 RI: 0.5 km, VE: 90% B-3 RI: 1.0 km, VE: 50% B-4 RI: 2.0 km, VE: 50% B-5 RI: 2.0 km, VE: 90%
Experiment C	Weighting Coefficient (constraints)	C-1 AWS (α_7): 10^3 C-2 Doppler Lidars (α_1): 10^3 C-3 LDAPS (α_8): 10^6

617

618   The impacts of the AWS cause negative values on the u-component winds in most areas at

619   800 m MSL in A-2 (Fig. 12c), especially in the western areas of the MHS site. Negative

620   contributions of the u-component winds produced by the AWS observations were restricted near

621   the surface, and the low wind speed area was extended to ~100 m above the surface (Fig. 12d).

622   The contributions of the u-component winds from the sounding observations were weak near the

623   DGW sounding site in A-3 (Figs. 12e and 12f). The impacts of u-component winds from the

624   LDAPS datasets were rather smaller in most of analysis area. in A-4 (Figs. 12g and 12h).

625   Relatively weak winds were presented near the surface from the results of A-5 (Figs. 12i and

626   12j). These results reflect that the additional constraints play crucial roles, especially at lower

627   layers. Furthermore, it is implied that the winds can be reasonably retrieved when additional

628   constraints are set in the modified version of WISSDOM.

629
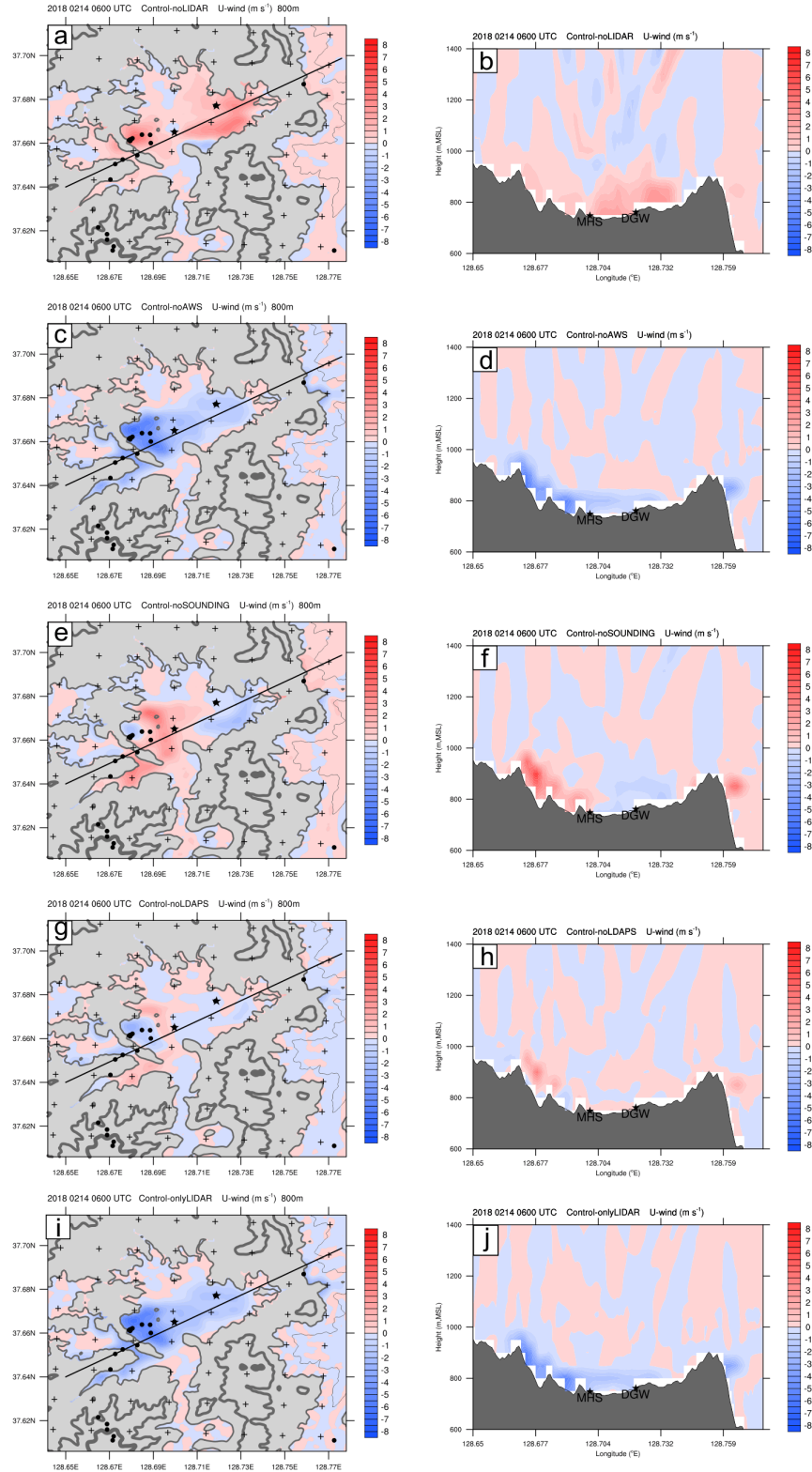
Figure 12. (a) The discrepancies in horizontal u-component winds between the control run and A-1 at 800 m MSL at 06:00 UTC on 14 Feb. 2018. (b) The same as (a) but for the vertical section along the black line in (a). (c) and (d) are the same as (a) and (b) but for A-2. (e) and (f) are the same as (a) and (b) but for A-3. (g) and (h) are the same as (a) and (b) but for A-4. (i) and (j) are the same as (a) and (b) but for A-5.

634

Averaged discrepancies in derived 3D winds for each vertical level in entire domain are shown in Fig. 13a. These results summarized a series of sensitivity tests if the WISSDOM synthesis lacks certain data inputs (i.e., A-1~A-5 in Experiment A) for derived u-, v- and w-component winds in the test domain. Overall, the maximum absolute value of averaged discrepancies for Experiment A are smaller than approximately 0.5 m s^{-1}, which are the discrepancies of the u-component winds for A-1 and A-2 located at 800 m MSL. Except for these values, the values of the derived u-, v- and w-component winds for A-1~A-2 are approximately smaller than 0.2 m s^{-1} from the surface up to the top in the test domain. Based on the results of A-5, relatively stronger values of derived u-component (exceeded -0.4 m s^{-1} at lower layers) can be obtained from the setting like old version of WISSDOM. The wind speed can be better modulated in modified version of WISSDOM when the Doppler lidar observations were adopted.

In addition, the discrepancies in derived 3D winds between sounding observations and QVP were also examined along the sounding tracks (Fig. 13b) and above the DGW site (Fig. 13c). Sounding observations played an essential role in the derived winds along its tracks. The maximum discrepancies of u- ~~(v)~~ component winds are exceeded by approximately -2 ~~(−1)~~ m s^{-1}, and v-component winds are exceeded by approximately -1 m s^{-1} if the WISSDOM synthesis lacks sounding observations. However, small discrepancies (nearly 0 m s^{-1}) were presented when the sounding ~~(lidar)~~ data were ~~(not)~~ implemented, and the lidar was not implemented at all levels in A-1. The peaks in the discrepancies manifested the potential impacts from the lidar and AWS. This may ~~be a~~ result ~~of~~ from lidar and ~~(AWS)~~ having ~~relativity~~ higher data coverage at ~1.4 and ~~(0.8)~~ km MSL, respectively (cf. Fig. 4). The discrepancies of sounding observation and control run in u- and v-component winds reveal relatively small values than the A-3 but similar to the other designs (purple lines in Figs. 13b). The maximum discrepancies between the derived winds and the QVP winds are approximately -4 and 4 ~~(−1 and 0)~~ m s^{-1} associated with u- and, v- ~~(w)~~ component winds, and -1 and 0 to the w-component winds. Generally, the results reveal similar trends in A-1~A-5, ~~which also implies~~ implying that all the inputs in the WISSDOM synthesis are

661 equally significant against the QVP. The QVP winds and control run discrepancies in u- and v-

662 component winds show similar values for all designs, but relatively small values can be obtained

663 in w-component winds (purple lines in Figs. 13c). In summary, the results of this experiment (cf.

664 Fig. 13) show that the lidar, sounding, and AWS data are more critical inputs than the LDAPS in

665 modified WISSDOM. Therefore, it will be beneficial if various inputs can be included in the

666 synthesis.
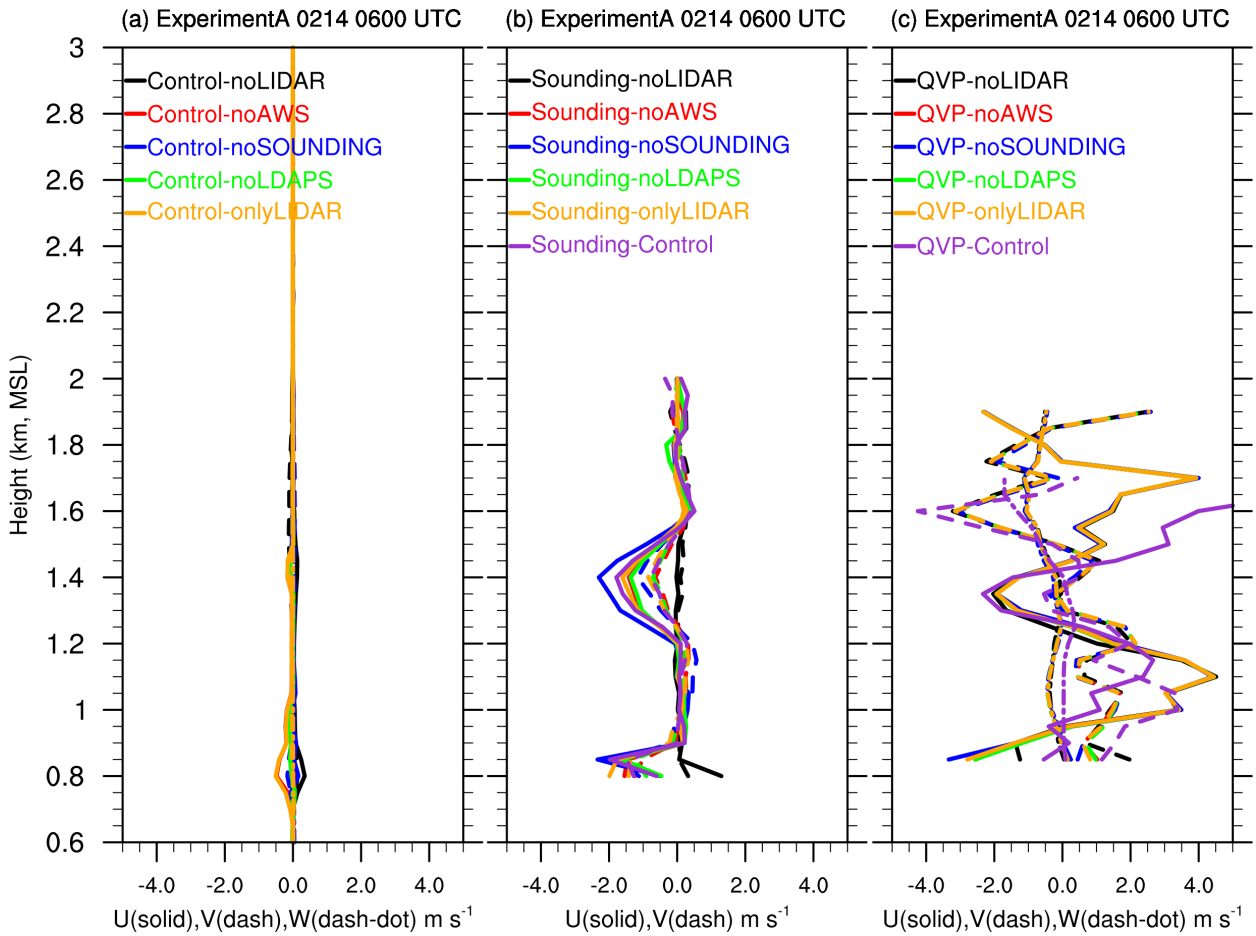
668 Figure 13. (a) Vertical profiles of averaged discrepancies of 3D winds for each design in Experiment A at 06:00

669   UTC on 14 Feb. 2018. The averaged discrepancies of u-, v- and w-component winds were plotted by solid, dash,

670   and dash-dot lines, and the black, red, blue, green and orange lines indicate A-1, A-2, A-3, A-4 and A-5,

671   respectively. (b) The same as (a) but for the discrepancies of sounding observations and u-, and v-component

672   winds and control run (purple lines). (c) The same as (~~a~~b) but for the discrepancies of QVP and w-component

673   winds.

674 **5.2 Radius of influence (RI) and vertical extension for the AWS (Experiment B)**

675   Experiment B was performed to check the discrepancies in 3D winds between the control run

676  and the different settings of RI and VE with the AWS observations. Because the average distance

677  is approximately 0.1 to 2 km between each AWS site, there were five designs (B-1~B-5) in

678  Experiment B with ranges of RI (VE) between 0.5 km (50%) and 2 km (90%). The details are

679  shown in Table 4. The horizontal u-component winds at 800 m MSL and the vertical structure of

680  Experiment B at one time step (06:00 UTC on 14 February 2018) are shown in Fig. 14. An

681  unusual circular area with positive discrepancies around the MHS site was depicted in B-1 (Figs,

682  14a and 14b), which may have been produced by the insufficient RI distance and VE (the circular

683  artefact is removed when increasing VE to 90%). Relatively smaller RI and VE values can only

684  include relatively less wind information if the distances are large between each AWS. Enlarging

685  the RI and VE are required to appropriately include more wind information from the AWS

686  observations. Figs. 14c and 14d show the results of B-2 as VE reached 90%. Although the unusual

687  circle vanished, there were discontinuities with negative values near the northern and southern

688  areas of the MHS site and positive areas surrounding the AWS (128.68°E, 37.66°N). The setting

689  of B-3 was similar to that of the control run except that the VE was 50%. The discrepancies were

690  relatively small, albeit dense AWS contributed even smaller negative values in the western areas

691  of the MHS sites (Figs. 14g and 14h). Obviously, positive discrepancies appeared near the

692  northern and southern areas of the MHS site in B-4 and B-5 (Figs. 14g-j). The impacts of the

693  AWS with various settings (B-1~B-5) on the discrepancies in u-component winds were both

694  restricted near the surface, even with a larger RI and high VE.

695
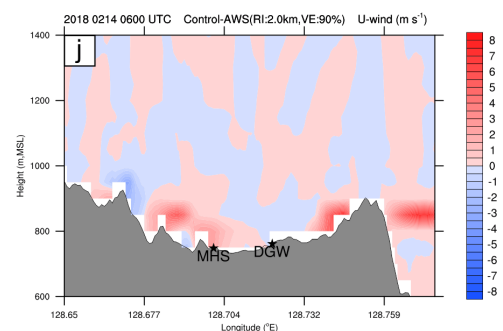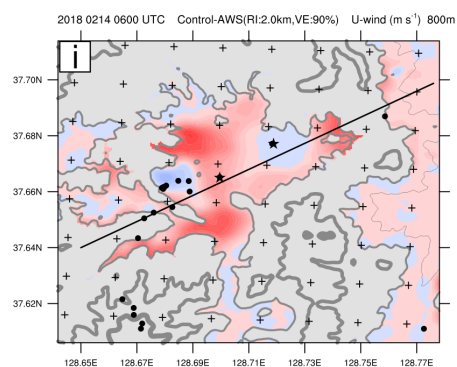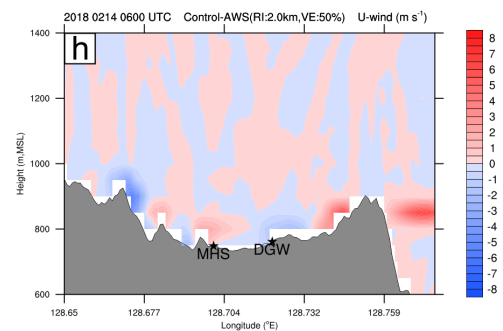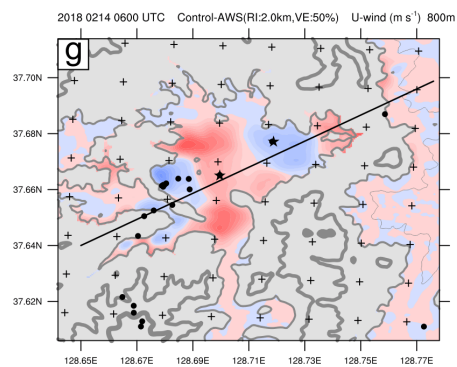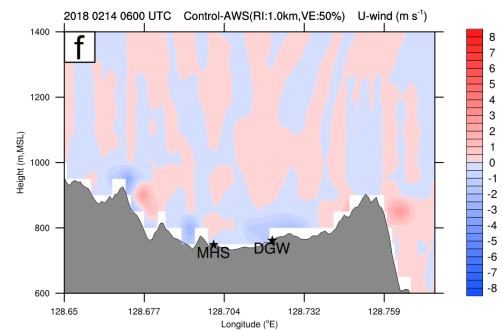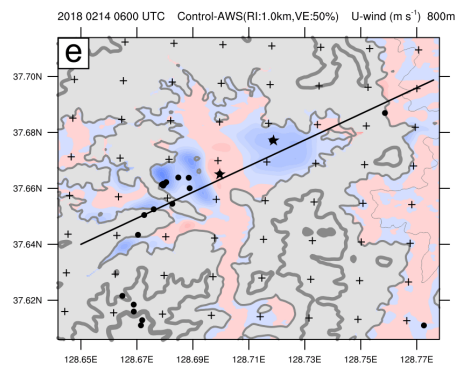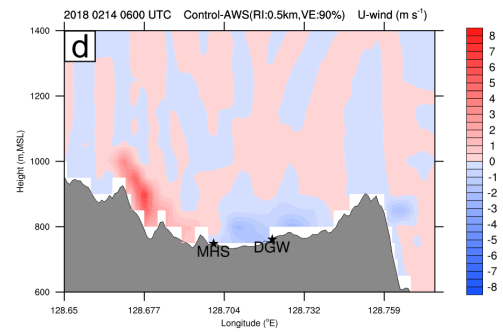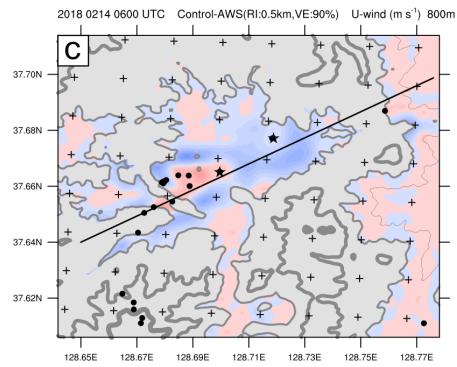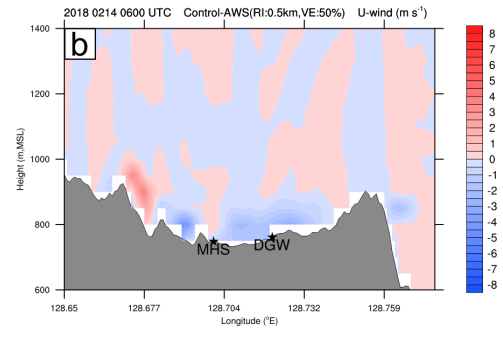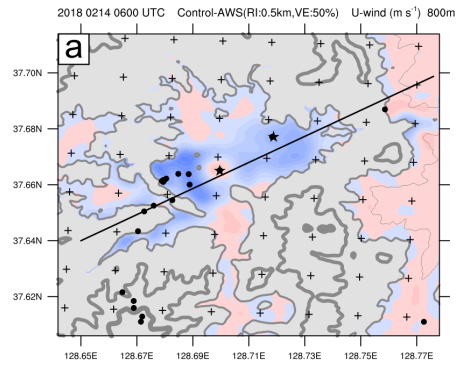
696 Figure 14. The same as Fig.12, but (a) and (b) for B-1. (c) and (d) are the same as (a) and (b) but for B-2. (e) and (f)
697   are the same as (a) and (b) but for B-3. (g) and (h) are the same as (a) and (b) but for B-4. (i) and (j) are the same
698   as (a) and (b) but for B-5.

699   Fig. 15a shows the vertical profiles of averaged discrepancies of derived 3D winds in

700 Experiment B. This figure summarizes the results of sensitivity testing with different settings of

701 the RI and VE in WISSDOM (i.e., B-1~B-5 in Experiment B, shown in Table 4) for derived u-,

702 v- and w-component winds in the test domain. The maximum discrepancies of u-component

703 winds in B-1, B-2 and B-3 were quite small at only 0.4, 0.3 and 0.2 m s^{-1}, respectively.

704 Nevertheless, the maximum discrepancies of u-component winds for B-4 and B-5 were larger

705 than 0.6 m s^{-1} and even exceeded ~1 m s^{-1}. Although the discrepancies in the u-component winds

706 in B-1 were small, the discrepancies in the v-component winds in B-1 reveal unusual patterns,

707 with larger positive values at ~1100 m MSL and negative values at ~1800 m MSL (black dashed

708 line in Fig. 15a), the possible reason is the minimizations of cost function are not converged well

709 because relatively few and weak v-component winds were included in B-1. Except for this value,

710 the maximum discrepancies of v-component winds were small for B-2~B-5, and the maximum

711 discrepancies of w-component winds were also small for all of Experiment B. Note that B-3

712 always has the smallest discrepancies with the derived 3D winds because the setting is quite

713 similar to the control run. Figs. 15b and 15c show the discrepancies of derived 3D winds between

714 the sounding observations, ~~and~~ QVP, and control run. Their patterns are similar to A-1~A5 (cf.

715 Figs. 13b and 13c), except there were relatively larger values of u- (v-) component winds at lower

716 layers (approximately −3 and 1 m s^{-1}) in B-1 (Fig. 15b). The v-component winds also presented

717 larger values (exceeded ~3 m s^{-1}) below ~1.2 km MSL compared with the QVP (Fig. 15c). The

718 conclusions indicate~~d~~ that the moderate setting (i.e., RI is 1 km) would be helpful to obtain ~~minor~~

719 smaller differences with the control run, sounding observations, and the QVP in this case. On the

720 other hand, the limited setting in experiment B (i.e., B-1) was ~~helpless~~not suitable. In addition,

721 the wind directions and speed should be dominated by terrain, and the implementation of AWS

722   data is crucial for the modified WISSDOM synthesis, especially in the lower layers.
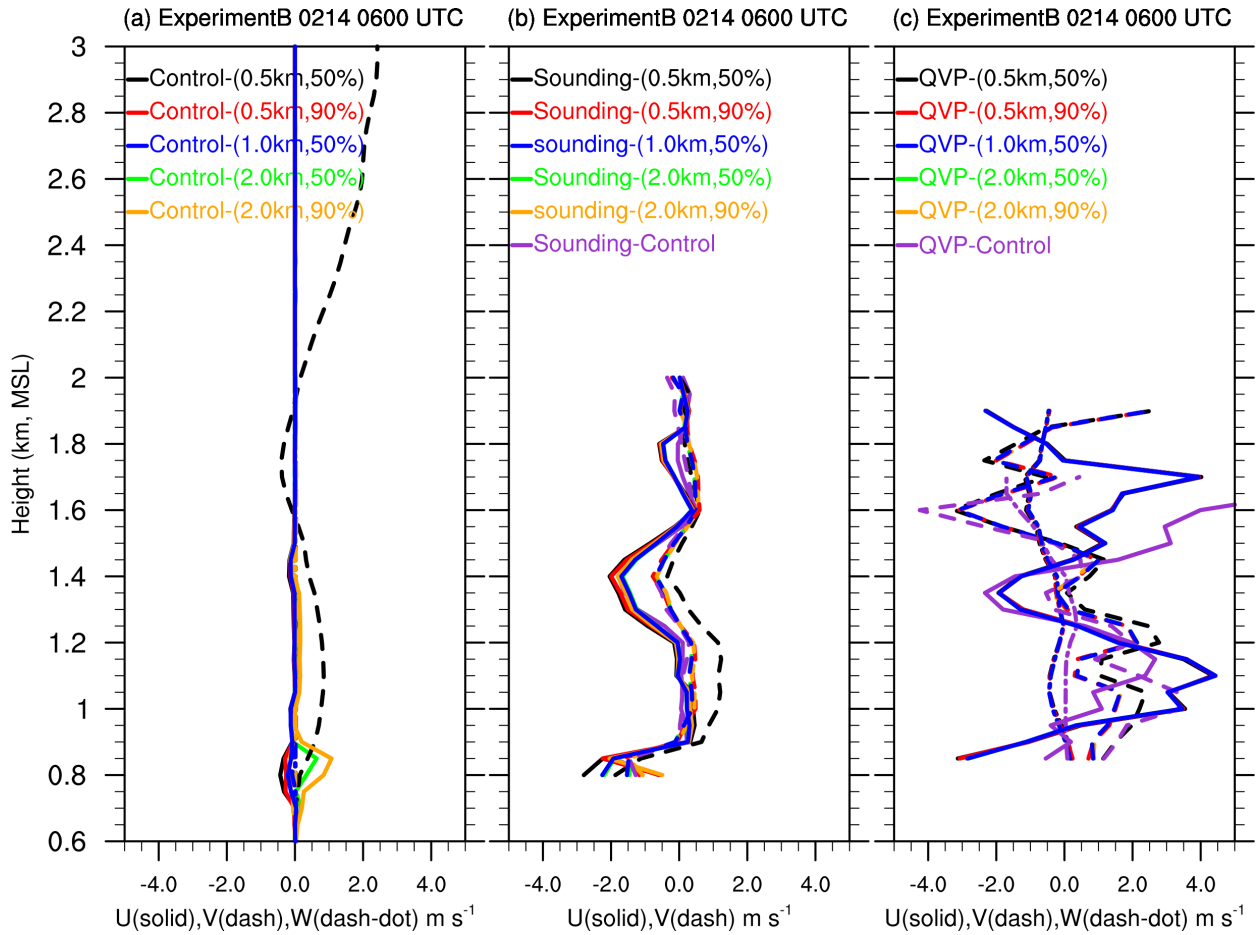
723

724   Figure 15. The same as Fig. 13. but for B-1~B-5.

5.3 Different weighting coefficients for the constraints (Experiment C)

726   Experiment C was designed to check the discrepancies in the derived u-component winds

727   between the control run and experimental runs with different weighting coefficients for each

728   constraint related to the AWS, lidar and LDAPS (corresponding to C-1, C-2 and C-3 in Table 4).

729   Originally, the weighting coefficients for the AWS and lidar observations were set to 10^6, and the

730   value was 10^3 for the LDAPS dataset (i.e., control run, Table 1). The results of Experiment C

731   show significant negative discrepancies in u-component winds near the surface in C-1, especially

732   in the areas next to the AWS (128.68°E, 37.66°N). The discrepancies for C-1 (Figs. 16a and 16b)

733   and C-2 (Figs. 16c and 16d) are similar to those for A-2 (Figs. 12c and 12d) and A-1 (Figs. 12a

734   and 12b), respectively. The inputs of AWS and lidar both contributed relatively weak impacts to

735 the WISSDOM synthesis when the weighting coefficient was set to 10^3. Irrational patterns were

736 depicted when the weighting coefficient of LDAPS inputs increased to 10^6, and larger and

737 positive discrepancies were crowded into most areas in the valley (i.e., C-3, Figs. 16e). Larger

738 and positive discrepancies existed only near the surface, and there were negative discrepancies

739 between approximately 1000 m and 1400 m (Fig. 16f). ~~Notably, s~~Significant ~~variances~~

740 ~~differences usually~~ often exist ~~ined~~ between the observations and reanalysis dataset~~s~~ due to

741 ~~various~~ the differing spatio-temporal resolutions. The results of scenario C-3 do not converge

742 well because there was a relatively more significant gradient between each input as their

743 weighting coefficients were set to be the same (i.e., 10^6). In this way, the effects of poor

744 convergences might be amplified ~~and superposed~~ with the AWS and lidar observations along the

745 sounding tracks. This may be a possible reason that artificial signals existed over the DGW site

746 in scenario C-3.

747  The vertical profiles of averaged discrepancies of derived 3D winds in Experiment C are

748 shown in Fig. 17a. Absolute values of the discrepancies in the u-, v- and w-component winds are

749 smaller than 1 m s^{-1}, except for the discrepancies in the v-component winds with low weighting

750 of the AWS observations (i.e., C-1) and the discrepancies in the u- and v-component winds with

751 the high weighted LDAPS (i.e., C-3). The discrepancies in the v-component winds in C-1

752 exceeded −5 m s^{-1} at ~1100 m MSL and were larger than −15 m s^{-1} above 2600 m MSL. These

753 unreasonable characteristics are also shown as the discrepancies in the v-component winds in B-

754 1 (cf. Fig. 15a). The discrepancies in the u- and v-component winds in C-3 are 15 m s^{-1} and 4 m

755 s^{-1}, respectively, in the layers between 700 and 900 m MSL. Alternative positive and negative

756 discrepancies in the range of −3 to 3 m s^{-1} for the u-component winds in C-3 were found above

757 1000 m MSL.

758  The discrepancies in between the derived 3D winds in Experiment C ~~between~~ and the

759 sounding observations and QVP, respectively, ~~in Experiment C~~ were also examined. Compared

760 to the sounding observations, more significant discrepancies in the u- and v-component winds

761 (exceed~~ing~~ed ~20 m s^{-1}) can be obtained when reducing ~~(increasing)~~ the weighting coefficients

762 of the AWS and increasing the weighting coefficients of the ~~(~~LDAPS~~)~~ data (Fig. 17b). However,

763 the impacts of lidar against the QVP are shown; their discrepancies are in the range of −1 to 2 m

764 s^{-1} for the u-component winds in C-2 (Fig. 17c). The discrepancies of sounding observations, the

765 QVP winds, and the control run were more minor than all designs in Experiment C (purple lines

766 in Figs. 17b and 17c). The conclusions reveal that the weighting coefficients of the AWS and

767 LDAPS ~~(lidar)~~ are ~~(moderately)~~ significantly sensitive to the derived winds, and the lidar is

768 moderately sensitive to the retrieved winds. Therefore, the weighting coefficients of LDAPS and

769 AWS are better to be 10^3 and 10^6~~not necessarily changed much.~~   in this case.
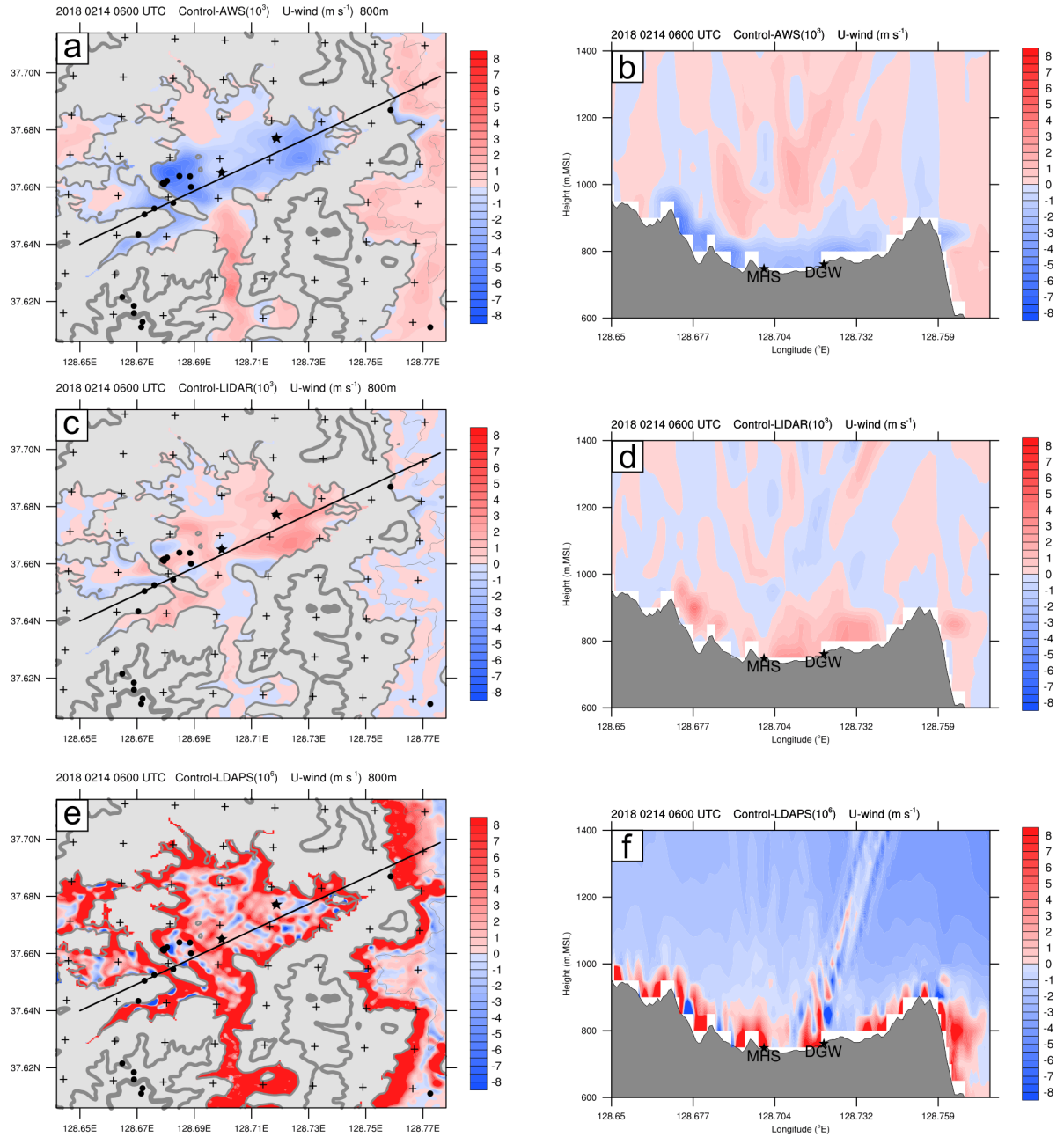
770
771 Figure 16. The same as Fig.12, but (a) and (b) for C-1. (c) and (d) are the same as (a) and (b) but for C-2. (e) and (f)
772   are the same as (a) and (b) but for C-3.
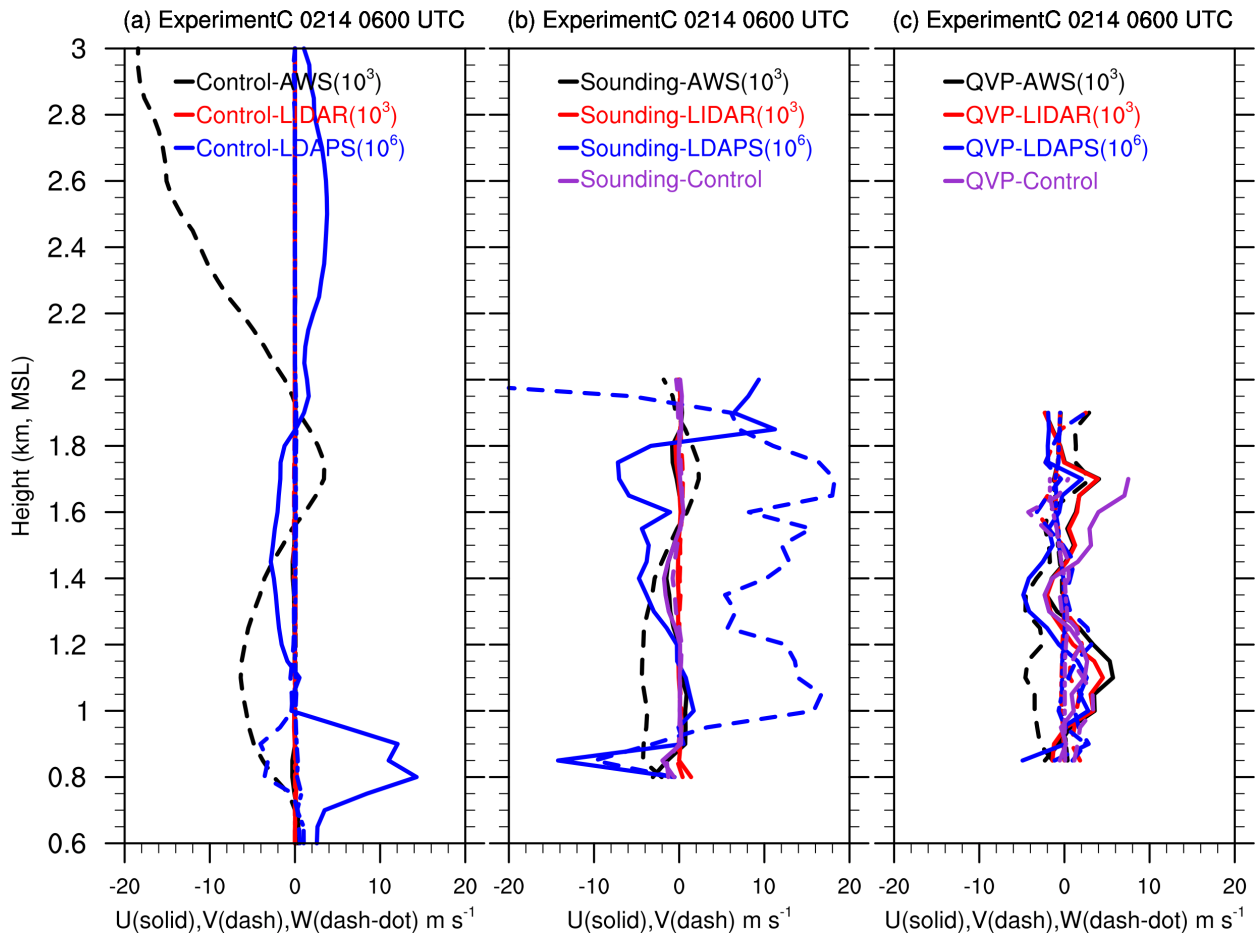
Figure 17. The same as Fig. 13 but for C-1~C-3.

6. Conclusion

A modified WISSDOM synthesis scheme was developed to derive high-quality 3D winds under clear-air conditions. The main difference from the original version is that multiple lidar observations were used in the modified version, replacing radar data. and hHigh-resolution 3D winds (50 m horizontally and vertically) were first derived in the modified WISSDOM scheme. In addition, the wind information was separated from the background in the modified version. Therefore, all available datasets were included as one of the constraints in the cost function in this study. The data implementation and the detailed principles of the modified WISSDOM were also elaborated. This modified WISSDOM scheme was performed over the TMR to retrieve 3D winds during a strong wind event during ICE-POP 2018. The performance was evaluated via a

785 series of sensitivity tests and compared with conventional observations.

786 The intercomparisons of horizontal winds during the entire research period reveal a relatively

787 high correlation coefficient between the optimal results of WISSDOM synthesis and sounding's

788 u- (v-) component winds exceeding 0.97 (0.87) at the DGW site. Furthermore, the average bias

789 is -0.78 m s^{-1} (0.09 m s^{-1}), and the RMSD is 1.77 m s^{-1} (1.65 m s^{-1}) for the u- (v-) component

790 winds. The intercomparisons of 3D winds between the WISSDOM synthesis and lidar QVP also

791 showed a higher correlation coefficient (0.84) for u-component winds, but a relatively smaller

792 correlation coefficient remained at 0.35 for v-component winds in this strong wind event. The

793 average bias (RMSD) of u-component winds is 2.83 m s^{-1} (3.69 m s^{-1}), and the average bias and

794 RMSD of v-component winds are 2.26 m s^{-1} and 2.92 m s^{-1}, respectively (cf. Table 2). Chen

795 (2019) analyzed the correlations between 3D winds derived from radar and observations in

796 several typhoon cases; the mean correlation coefficient ranged from 0.56 to 0.86, and the RMSD

797 was between 1.13 and 1.74 m s^{-1}. Compared to their results, only u-component winds have

798 relatively higher correlation coefficients, but the RMSD values are slightly higher in this study,

799 which may have been caused by the high variability in westerly winds associated with the moving

800 LPS. The statistical error results of the winds between the optimal results of WISSDOM synthesis

801 and observations show a good performance of the retrieved 3D winds in this strong wind event

802 (Table 3). Generally, the median values of wind directions are within ~10 degrees. Compared

803 with lidar QVP (sounding observations) above the DGW site, the median values of the wind

804 speed are approximately -1~3 m s^{-1} (-1~0.5 m s^{-1}), and the vertical velocity is within -0.2~0.6

805 m s^{-1};. Compared with lidar QVP (sounding observations) above the DGW site, the interquartile

806 rangeIQR of wind directions is -10~5 (0-2.5) degrees, the wind speed is approximately -4~4 m

807 s^{-1} (-1~3 m s^{-1}), and the vertical velocity is -0.8~0.8 m s^{-1}. The summaries of the correlation

808 coefficients, average bias, the RMSD, and range of statistical errors are shown in the schematic

809 diagrams as Figs. 18a and 18b.
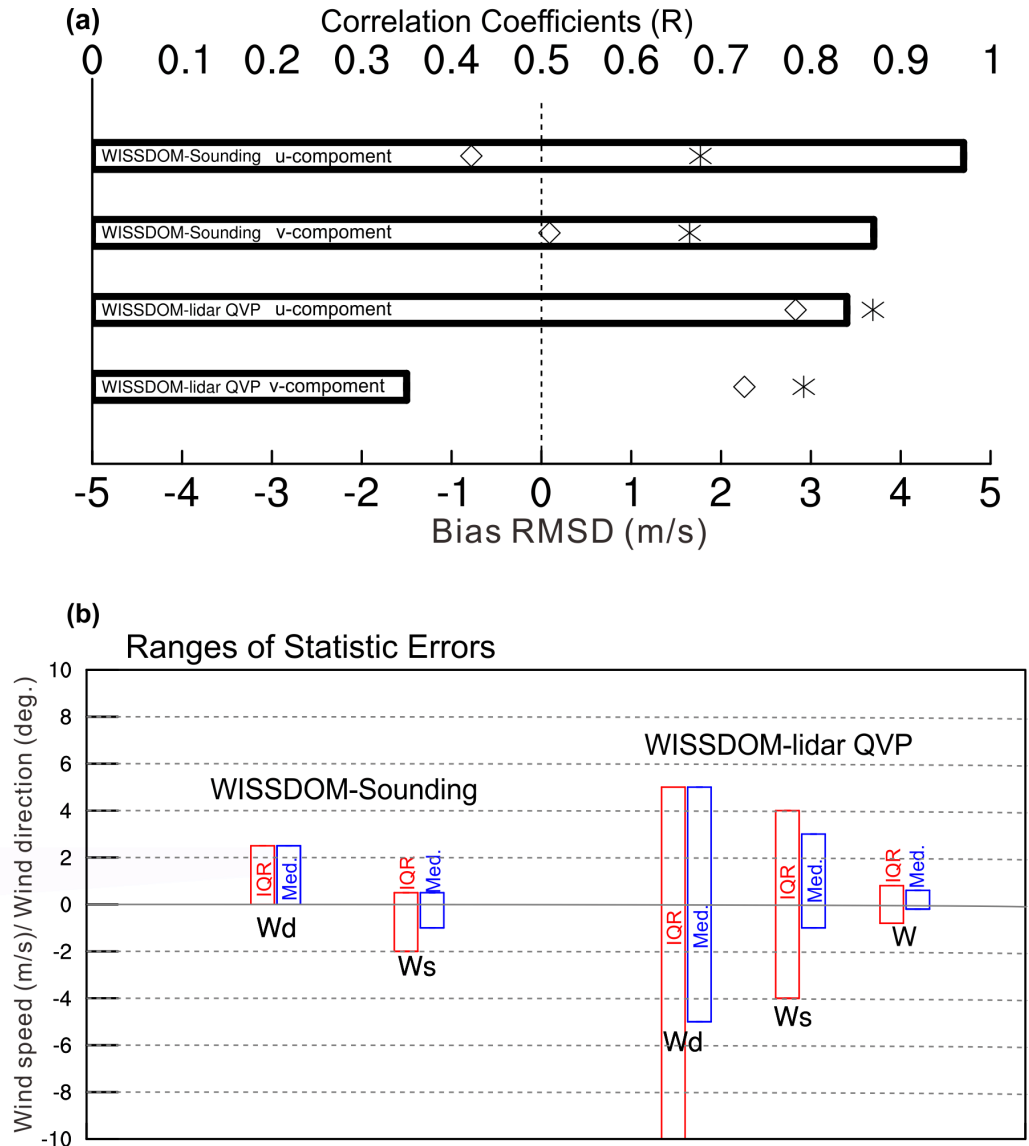
Figure 18. Schematic diagrams for the results of intercomparisons on (a) the correlation coefficients (R, histograms),

the average bias (marked as diamonds), and the RMSD (marked as asterisks). (b) The ranges of statistic error for

the IQR (red boxes) and median values (blue boxes). The wind directions, wind speed and w-component winds

are denoted as Wd, Ws, and W respectively.

A control run (see the basic setting in Table 1) was set to explore the importance of acquired

observation datasets, various distances of RI, VE from the AWS observations, and the weighting

coefficient for each constraint (i.e., Experiments A-C, Table 4). The results of Experiment A

show that the lidar and AWS play critical roles in the derived horizontal winds, and the lidars

(AWS) provided positive (negative) contributions in stronger (weaker) wind speeds near the

surface. The sounding and the LDAPS provided relatively smaller impacts on the derived

horizontal winds from the WISSDOM synthesis. In Experiment B, minor discrepancies in 3D

822   winds were depicted when the RI (VE) was set to 1 km (50%), which indicated that the optimal

823   setting of the RI is 1 km. However, there were larger discrepancies in 3D winds (from -0.4 m s^{-1}

824   to ~1 m s^{-1}) when the RI was set at 0.5 km and 2 km, and the VE was set between 50% and 90%

825   (cf. Fig. 15). In Experiment C, significant discrepancies in 3D winds appeared by decreasing

826   (raising) the weighting coefficient from the AWS observations (LDPAS datasets). Relatively

827   reasonable winds can be derived with ~~optimal settings in modified WISSDOM, and~~ the setting

828   of 1 km in RI and 90% ~~(50%)~~ in VE ~~is also recommended~~ over complex terrain (i.e., the same

829   setting as the control run) ~~(flat surface)~~. These sensitivity tests will help verify the impacts against

830   various scenarios and observational references in this area~~. The conclusions can also be a good~~

831   ~~reference for deciding the best locations to deploy the instruments~~.

832   This study demonstrated that reasonable patterns of 3D winds were derived by the modified

833   WISSDOM synthesis scheme in a strong wind event. Reasonable winds can be retrieved from

834   modified WISSDOM with sufficient coverage from the data, a moderate weighting function, and

835   appropriate implementation from different datasets. In the future, many cases are required to

836   check the performance of this modified WISSDOM scheme with different synoptic weather

837   systems under clear-air conditions in different seasons. In addition, knowing the detailed

838   kinematic fields will help us to identify where the flow accelerates/decelerates over complex

839   terrain. Thus, the possible mechanisms of extremely strong winds in South Korea will be well

840   documented through combinations with derived dynamic fields (Tsai et al., 2018, 2022),

841   thermodynamic fields (Liou et al., 2019), observations and simulations. The detailed wind

842   structures can be well documented for any meteorological phenomena in clear-air conditions

843   (e.g., land−sea breezes, microdownbursts, nonprecipitation low-pressure systems, etc.) via a

844   modified version of WISSDOM. It also has broad applications in site surveys of wind turbines,

845   wind energy, monitoring wildfires, outdoor sports in mountain ranges, and aviation security.

846   *Code and data availability.* The scanning Doppler lidars, AWS, and sounding data used in this
847   study are available through zenodo: https://doi.org/10.5281/zenodo.6537507. The LDAPS
848   dataset is freely available from the KMA website (https://data.kma.go.kr).

849

850   *Acknowledgments.* This work was supported by the National Research Foundation of Korea (NRF)
851   grant funded by the Korea government (MSIT) (No. 2021R1A4A1032646) and by the Korea
852   Meteorological Administration Research and Development Program under Grant KMI2022-
853   00310.

854

855   *Author contributions.* This work was made possible by contribution from all authors.
856   Conceptualization, CLT, GWL; methodology, CLT, YCL, and KK; software, CLT, YCL, and
857   KK; validation, KK, YCL, and GWL; formal analysis, CLT, and KK; investigation, CLT, and
858   GWL; writing—original draft preparation, CLT; writing—review and editing, GWL, YCL and
859   KK; visualization, CLT; supervision, GWL; funding acquisition, GWL. All authors have read
860   and agreed to the published version of the manuscript.

861

862   *Competing interests.* The authors declare that they have no conflict of interest.

863

864   *Special issue statement.* This article is part of the special issue "Winter weather research in
865   complex terrain during ICE-POP 2018 (International Collaborative Experiments for
866   Pyeongchang 2018 Olympic and Paralympic winter games) (ACP/AMT/GMD inter-journal SI)".
867   It is not associated with a conference.

868
869

870 **References**

871 Armijo, L.: A theory for the determination of wind and precipitation velocities with Doppler

872   radars. J. Atmos. Sci., 26, 570–573. 1969.

873 Bell, M. M., Montgomery, M. T., and Emanuel, K. A.: Air–sea enthalpy and momentum

874   exchange at major hurricane wind speeds observed during CBLAST, *J. Atmos. Sci.*, **69**,

875   3197–3222, https://doi.org/10.1175/JAS-D-11-0276.1, 2012.

876 Bell, T. M., Klein, P., Wildmann, N., and Menke, R.: Analysis of flow in complex terrain using

877   multi-Doppler lidar retrievals, *Atmos. Meas. Tech.*, **13**, 1357–1371,

878   https://doi.org/10.5194/amt-13-1357-2020, 2020.

879 Browning, K. A., and Wexler, R..: The Determination of Kinematic Properties of a Wind Field

880   Using Doppler Radar, *J. Appl. Meteorol.*, **7**, 105–113, https://doi.org/10.1175/1520-

881   0450(1968)007<0105:TDOKPO>2.0.CO;2, 1968.

882 Chen, Y.-A.: Verification of multiple-Doppler-radar derived vertical velocity using profiler data

883   and high resolution examination over complex terrain, M.S. thesis, National Central

884   University, 91 pp., 2019.

885 Choi, D., Hwang, Y., Lee, YH.: Observing Sensitivity Experiment Based on Convective Scale

886   Model for Upper-air Observation Data on GISANG 1 (KMA Research Vessel) in Summer

887   2018. *Atmosphere*, **30**, 17–30, 2020 (Korean with English abstract).

888 Cha, T.-Y. and Bell, M. M.: Comparison of single-Doppler and multiple-Doppler wind retrievals

889   in Hurricane Matthew (2016), *Atmos. Meas. Tech.*, **14**, 3523–3539,

890   https://doi.org/10.5194/amt-14-3523-2021, 2021.

891 Choukulkar, A., Brewer, W. A., Sandberg, S. P., Weickmann, A., Bonin, T. A., Hardesty, R. M.,

892   Lundquist, J. K., Delgado, R., Iungo, G. V., Ashton, R., Debnath, M., Bianco, L., Wilczak,

893   J. M., Oncley, S., and Wolfe, D.: Evaluation of single and multiple Doppler lidar

894   techniques to measure complex flow during the XPIA field campaign, *Atmos. Meas. Tech.*,

895   **10**, 247–264, https://doi.org/10.5194/amt-10-247-2017, 2017.

896   Colle, B. A., and Mass, C. F.: High-Resolution Observations and Numerical Simulations of

897   Easterly Gap Flow through the Strait of Juan de Fuca on 9–10 December 1995. *Mon. Wea.*

898   *Rev.*, **128**, 2398–2422,

899   Cressman, G. P.: An operational objective analysis system. *Mon. Wea. Rev.*, **87**, 367–374, 1959.

900   Gao, J., Droegemeier, K. K., Gong, J., and Xu, Q.: A method for retrieving mean horizontal wind

901   profiles from single-Doppler radar observations contaminated by aliasing, *Mon. Wea.*

902   *Rev.*, **132**, 1399–1409, https://doi.org/10.1175/1520-

903   0493(2004)132<1399:AMFRMH>2.0.CO;2, 2004.

904   Hill, M., R. Calhoun, H. J. S. F., Wieser, A., Dornbrack, A., Weissmann, M., Mayr, G., and

905   Newsom, R.: Coplanar Doppler lidar retrieval of rotors from T-REX, *J. Atmos. Sci.*, **67**,

906   713–729, 2010.

907   Jou, B. J.-D., Lee, W.-C., Liu, S.-P., and Kao, Y.-C.: Generalized VTD retrieval of atmospheric

908   vortex kinematic structure. Part I: Formulation and error analysis, *Mon. Weather Rev.*,

909   **136**, 995–1012, https://doi.org/10.1175/2007MWR2116.1, 2008.

910   Kim D.-J., Kang G., Kim D.-Y., Kim J.-J.: Characteristics of LDAPS-Predicted Surface Wind

911   Speed and Temperature at Automated Weather Stations with Different Surrounding Land

912   Cover and Topography in Korea. *Atmosphere*, **11**, 1224.

913   https://doi.org/10.3390/atmos11111224, 2020.

914   Kim, J.-H., R. D. Sharman, R. D., Benjamin, S., Brown, J., Park, S.-H. and Klemp, J.:

915   Improvement of Mountain Wave Turbulence Forecast in the NOAA's Rapid Refresh

916   (RAP) Model with Hybrid Vertical Coordinate System, *Weather Forecast*, **34(6)**, 773-

917   780, https://doi.org/10.1175/WAF-D-18-0187.1, 2019.

918   Kim, K., Lyu, G., Baek, S., Shin, K., and Lee, G.: Retrieval and Accuracy Evaluation of

919   Horizontal Winds from Doppler Lidars during ICE-POP 2018, *Atmos.*, **32**, 163–178,

920   https://doi.org/10.14191/Atmos.2022.32.2.161, 2022.

921   Lee, J., Seo, J., Baik, J., Park, S., and Han, B.: A Numerical Study of Windstorms in the Lee of

922   the Taebaek Mountains, South Korea: Characteristics and Generation

923   Mechanisms. *Atmosphere*, **11**, 431. https://doi.org/10.3390/atmos11040431, 2020.

924   Lee, J.- T., Ko, K.- Y., Lee, D.- I., You, C.- H., and Liou, Y.- C.: Enhancement of orographic

925   precipitation in Jeju Island during the passage of Typhoon Khanun (2012), *Atmos. Res.*,

926   **201**, 1245–1254. https://doi.org/10.1016/j.atmosres.2017.10.013, 2017.

927   Lee, W.-C., Marks, F. D., and Carbone, R. E.: Velocity track display – A technique to extract

928   real-time tropical cyclone circulations using a single airborne Doppler radar, *J. Atmos.*

929   *Ocean. Tech.*, **11**, 337–356, https://doi.org/10.1175/1520-

930   0426(1994)011<0337:VTDTTE>2.0.CO;2, 1994

931   Lee, W.-C., Jou, B. J.-D., Chang, P.-L., and Deng, S.- M.: Tropical cyclone kinematic structure

932   derived from single-Doppler radar observations. Part I: Interpretation of Doppler velocity

933   patterns and the GBVTD technique, *Mon. Weather Rev.*, **127**, 2419–2439,

934   https://doi.org/10.1175/1520-0493(1999)127<2419:TCKSRF>2.0.CO;2, 1999.

935   Liou, Y.-C., Wang, T.-C. C., Lee, W.-C., and Chang, Y.-J.: The retrieval of asymmetric tropical

936   cyclone structures using Doppler radar simulations and observations with the extended

937   GBVTD technique, *Mon. Weather Rev.*, **134**, 1140–1160,

938   https://doi.org/10.1175/MWR3107.1, 2006.

939   Liou, Y., and Chang, Y.: A Variational Multiple–Doppler Radar Three-Dimensional Wind

940   Synthesis Method and Its Impacts on Thermodynamic Retrieval. *Mon. Wea. Rev.*, **137**,

941   3992–4010, https://doi.org/10.1175/2009MWR2980.1, 2009.

942   Liou, Y., Chang, S., and Sun, J.: An Application of the Immersed Boundary Method for

943   Recovering the Three-Dimensional Wind Fields over Complex Terrain Using Multiple-

944   Doppler Radar Data. *Mon. Wea. Rev.*, **140**, 1603–1619, https://doi.org/10.1175/MWR-D-

945   11-00151.1, 2012.

946   Liou, Y., Chen Wang, T., Tsai, Y., Tang, Y., Lin, P., and Lee, Y.: Structure of precipitating systems

947   over Taiwan's complex terrain during Typhoon Morakot (2009) as revealed by weather

948   radar and rain gauge observations, *J. Hydrology*, **506**, 14-25.

949   https://doi.org/10.1016/j.jhydrol.2012.09.004, 2013.

950 Liou, Y., Chiou, J., Chen, W., and Yu, H.: Improving the Model Convective Storm Quantitative

951   Precipitation Nowcasting by Assimilating State Variables Retrieved from Multiple-

952   Doppler Radar Observations. *Mon. Wea. Rev.*, **142**, 4017–4035,

953   https://doi.org/10.1175/MWR-D-13-00315.1, 2014.

954 Liou, Y., Chen Wang, T., and Huang, P.: The Inland Eyewall Reintensification of Typhoon

955   Fanapi (2010) Documented from an Observational Perspective Using Multiple-Doppler

956   Radar and Surface Measurements. *Mon. Wea. Rev.*, **144**, 241–261,

957   https://doi.org/10.1175/MWR-D-15-0136.1, 2016.

958 Liou, Y. C., Yang, P. C., and Wang, W. Y.: Thermodynamic recovery of the pressure and

959   temperature fields over complex terrain using wind fields derived by multiple-Doppler

960   radar synthesis. Mon. Wea. Rev., **147(10)**, 3843-3857, https://doi.org/10.1175/MWR-D-

961   19-0059.1, 2019.

962 Mass, C. F., and Ovens, D.: The Northern California Wildfires of 8–9 October 2017: The Role

963   of a Major Downslope Wind Event. *Bull. Amer. Meteor. Soc.*, **100**, 235–256,

964   https://doi.org/10.1175/BAMS-D-18-0037.1, 2019.

965 Mohr, C. G., and Miller, L. J. : CEDRIC—A software package for Cartesian Space Editing,

966   Synthesis, and Display of Radar Fields under Interactive Control. Preprints, *21st Conf. on*

967   *Radar Meteorology,* Edmonton, AB, Canada, Amer. Meteor. Soc., 569–574, 1983.

968 Oue, M., Kollias, P., Shapiro, A., Tatarevic, A., and Matsui, T.: Investigation of observational

969   error sources in multi-Doppler-radar three-dimensional variational vertical air motion

970   retrievals, *Atmos. Meas. Tech.*, **12**, 1999–2018, https://doi.org/10.5194/amt-12-1999-

971   2019, 2019.

972 Park, J.-R., Kim, J.-H., Shin, Y., Kim, S.-H., Chun, H.-Y., Jang, W., Tsai, C.-L. and Lee, G.: A

973   numerical simulation of a strong windstorm event in the Taebaek Mountain Region in

Korea during the ICE-POP 2018, *Atmos. Res.*, **272**, 106158, https://doi.org/10.1016/j.atmosres.2022.106158.

Päschke, E., Leinweber, R., and Lehmann, V.: An assessment of the performance of a 1.5 μm Doppler lidar for operational vertical wind profiling based on a 1-year trial, *Atmos. Meas. Tech.*, **8**, 2251–2266, https://doi.org/10.5194/amt-8-2251-2015, 2015.

Reed, T. R.: GAP WINDS OF THE STRAIT OF JUAN DE FUCA. *Mon. Wea. Rev.*, **59**, 373–376, https://doi.org/10.1175/15200493(1931)59<373:GWOTSO>2.0.CO;2, 1931.

Ryzhkov, A., Zhang, P., Reeves, H., Kumjian, M., Tschallener, T., Trömel, S., and Simmer, C.: Quasi-Vertical Profiles—A New Way to Look at Polarimetric Radar Data. *J. Atmos. Oceanic Technol.*, **33**, 551–562, https://doi.org/10.1175/JTECH-D-15-0020.1, 2016.

Tsai, C., Kim, K., Liou, Y., Lee, G., and Yu, C.: Impacts of Topography on Airflow and Precipitation in the Pyeongchang Area Seen from Multiple-Doppler Radar Observations. *Mon. Wea. Rev.*, **146**, 3401–3424, https://doi.org/10.1175/MWR-D-17-0394.1, 2018.

Tsai, C.-L., Kim, K., Liou, Y.-C., Kim, J.-H., Lee, Y., and Lee, G.: Orographic-induced strong wind associated with a low-pressure system under clear-air condition during ICE-POP 2018, *J. Geophys. Res. Atmos.*, **127**, e2021JD036418. https://doi.org/10.1029/2021JD036418, 2022.

Tseng, Y., and Ferziger, J.: A ghost-cell immersed boundary method for flow in complex geometry. *J. Comput. Phys.*, **192**, 593–623, https://doi.org/10.1016/j.jcp.2003.07.024. 2003.

Yu, C.- K., and Bond, N. A.: Airborne Doppler observations of a cold front in the vicinity of Vancouver Island. Mon. Wea. Rev., 130, 2692-2708, https://doi.org/10.1175/1520-0493(2000)128<1577:ADOOAL>2.0.CO;2, 2002.

Yu, C., and Tsai, C.-L.: Surface Pressure Features of Landfalling Typhoon Rainbands and Their Possible Causes. *J. Atmos. Sci.*, **67**, 2893–2911, https://doi.org/10.1175/2010JAS3312.1,

1000   2010.

1001   Yu, C.-K., and Tsai, C.-L. : Structural and surface features of arc-shaped radar echoes along an

1002   outer tropical cyclone rainband. *J. Atmos. Sci.*, **70**, 56– 72. https://doi.org/10.1175/JAS-

1003   D-12-090.1, 2013.

1004   Yu, C.-K., and Tsai, C.-L.: Structural changes of an outer tropical cyclone rain band encountering

1005   the topography of northern Taiwan. *Q. J. R. Meteorol. Soc*, **143**, 1107–1122.

1006   https://doi.org/10.1002/qj.2994, 2017.

1007   Yu, C.- K., and Jou, B. J.-D.: Radar observations of diurnally forced, offshore convective lines

1008   along the southeastern coast of Taiwan. Mon. Wea. Rev., 133, 1613-1636,

1009   https://doi.org/10.1175/MWR2937.1, 2005.

1010   Yu, C.-K., Cheng, L.-W., Wu, C.-C., and Tsai, C.-L.: Outer Tropical Cyclone Rainbands

1011   Associated with Typhoon Matmo (2014). *Mon. Wea. Rev.*, **148**, 2935–2952,

1012   https://doi.org/10.1175/MWR-D-20-0054.1, 2020.